Characterisation and Toxicity Assessment of Metal Ion-Enriched Nanoparticles

Erik Lundberg & Nicolai Gripberg
Department of Chemistry | Faculty of Engineering | Lunds Universitet
Master of Science Thesis 2024

LUNDS
UNIVERSITET

Characterization and Toxicity Assessment of Metal Ion-Enriched Nanoparticles

by

Nicolai Gripberg
Erik Lundberg

Department of Chemical Engineering, Lund University
Supervisor: Martin Ek Rosén
Examiner: Reine Wallenberg

In collaboration with Spago Nanomedical, Lund
Supervisor: Oskar Axelsson

June 2024

Abstract

Cancer remains one of the main challenges in healthcare, with profound global impact both in terms of morbidity and mortality. Spago Nanomedical is a Swedish company that has developed innovative metal-ion enriched nanoparticle-based therapies for cancer treatment and diagnosis. These nanoparticles have shown great promise and are currently undergoing clinical trials, however, there persists a desire to further investigate the bio-distribution of the particles. The limitation of the current nanoparticles is that they are incorporating a low amount of metal with relatively low atomic number, resulting in insufficient contrast in computed tomography scan (CT). This study focuses on enhancing the contrast of these nanoparticles for improved distribution studies by incorporating elements with higher atomic numbers such as bismuth, gadolinium, hafnium, and lutetium. The report presents an investigation of the metal-loading, characterization, and cytotoxicity assessment of the nanoparticles, laying the foundation for potential biomedical applications. Through a combination of analytical techniques including inductively coupled plasma optical emission spectrometry (ICP-OES), dynamic light scattering (DLS), size exclusion chromatography (SEC), transmission electron microscopy (TEM), and cytotoxicity assays, the successful loading of high atomic number metals into nanoparticles was demonstrated. The nanoparticles exhibited consistent size distribution and morphology, with the incorporation of metal ions theoretically enhancing their contrast properties for potential use in CT-scans. Cytotoxicity assessments revealed minimal toxicity of the metal-loaded nanoparticles, supporting their safety for potential *in vivo* applications. These findings lay a solid foundation for further research regarding the clinical applications of metal-loaded nanoparticles, including distribution studies.

Acknowledgements

First, we would like to express our sincere gratitude to our on-site supervisor Oskar Axelsson for providing excellent support and feedback throughout the project. We also wish to thank Martin Ek Rosén for his consistent participation and valuable contributions. Additionally, we appreciate Reine Wallenberg for assuming the role of examiner. Finally, we would like to thank all the colleagues at Spago Nanomedical and Crispin Hetherington whose collaborative efforts have been instrumental in the completion of this thesis.

Pioneering Cancer Diagnosis and Therapy using Metal Loaded Nanoparticles

Imagine tiny particles so small they're invisible to the naked eye, yet powerful enough to potentially revolutionize cancer diagnosis and treatment. That's precisely what researchers at Spago Nanomedical have been working on. In collaboration with Spago Nanomedical, we detail our successful loading of these so-called nanoparticles with metals, theoretically enhancing their contrast for imaging techniques like Computed Tomography scans.

With approximately 10 million people succumbing to cancer annually worldwide, the need for more accurate diagnostic tools and effective treatment strategies has never been more urgent. Spago Nanomedical, an innovative research company, has developed a nanoparticle-based product to combat cancer cells. When injected, the product functions by selectively binding to cancer tissue, leading to an accumulation of nanoparticles in the tumors. While these nanoparticles are designed to selectively accumulate in cancer tissue, the precise mechanism of how and where the particles end up in the body is yet to be completely understood. To address this knowledge gap, this thesis aimed to improve the contrast in distribution studies by loading the nanoparticles with new metals.

The project involved loading nanoparticles with the metals bismuth, gadolinium, hafnium and lutetium. These loaded particles were then characterized using several analytical techniques to ensure that the size, shape and chemical composition was suitable. Yet, safety remains paramount, motivating the assessment of toxicity. This was done by subjecting cell cultures to increasing concentrations of our nanoparticles and recording their potential harm.

Through the procedures described above, our research confirmed that these metal-loaded nanoparticles are successfully loaded with the metals, theoretically leading to greater contrast in computed tomography. Our results also show that the particles pose minimal risk to cells, making them promising candidates for further studies and potential use in medical applications. Our findings open doors for more accurate visualization of where the nanoparticles end up within the body of a patient, paving the way for improved diagnostics and targeted therapies.

Contents

1 List of abbreviations

Abbreviation	Definition
AEM	Analytical Electron Microscopy
CT	Computer Tomography
CTEM	Conventional Transmission Electron Microscopy
DLS	Dynamic Light Scattering
ELSD	Evaporative Light-Scattering Detector
EELS	Electron Energy-Loss Spectrometry
EPR	Enhanced Permeability and Retention
GPC	Gel Permeation Chromatography
ICP-OES	Inductively-coupled Plasma Optical Emission Spectrometry
MQ water	Milli-Q Water
PEG	Polyethylene Glycol
SDS	Sodium Dodecyl Sulfate
SEC	Size Exclusion Chromatography
STEM	Scanning Transmission Electron Microscope
TEM	Transmission Electron Microscope
XEDS	X-ray Energy Dispersive Spectrometry

2 Introduction

Cancer, with its widespread presence and severe effects, stands as one of the most pressing challenges in modern medicine. In 2022, the global landscape of cancer was marked by an estimated 20 million new cases diagnosed worldwide, culminating in 9.7 million lives lost [1]. Within the United States alone, the impact of cancer is profound, with an anticipated 1.9 million new cases diagnosed and an estimated 610,000 cancer related deaths in 2022 [2]. Beyond the mortality, cancer imposes a substantial economic burden, encompassing direct medical costs, loss of productivity, and socioeconomic inequalities. Such financial strains not only impact individuals and families but also healthcare systems and societal structures.

Over the years, advancements in cancer research has improved patient outcomes and survival rates. These advancements are a testament to the collective dedication within the medical and scientific communities, including large influential companies, but also to small innovative companies such as Spago Nanomedical.

Spago Nanomedical is a Swedish nanomedicine company focusing on the development of novel functional nanoparticles for selective cancer therapies. The company's proprietary technology platform is based on polymeric nanoparticles loaded with metal ions. These particles, carrying the radioactive lutetium isotope ^{177}Lu, aim to treat diseases like cancer through selective irradiation, working as a radiopharmaceutical treatment against several types of solid soft tissue tumors.

The tumor selectivity of the nanoparticles is possible due to the Enhanced Permeability and Retention effect (EPR effect). The EPR effect refers to an accumulation of macromolecules in cancer tissue, due to increased permeability of the capillary walls in the tumor. The nanoparticle is designed to optimally utilize the EPR effect and have high selectivity and retention time in tumor tissue.

As the whole technology platform is based on the tumor selective properties, it is crucial to obtain highly accurate distribution characteristics of the nanoparticles. Prior *in vivo* investigations have assessed the biodistribution of particles. Nonetheless, there persists a desire to determine the distribution with enhanced precision to achieve a deeper understanding of the nanoparticles' distribution.

2.1 Goal and Objectives

The current challenge lies in the nanoparticles containing relatively low amounts of metal-ions, resulting in low CT contrast. To enhance contrast in future distribution studies, the main objective is to explore and evaluate the nanoparticles loading capacity of elements with high atomic num-

bers. This will be done through alteration and investigation of the metal incorporation process, and the consequent characteristics of the metal-loaded nanoparticle.

Ultimately, the goal of this thesis is to lay a scientific foundation for future distribution studies of the nanoparticles enriched with metal ions. The hope is that the findings of this project will allow future experiments where the nanoparticles' *in vivo* distribution characteristics can be more accurately determined. Since the goal is to use these metal-ion loaded nanoparticles in an *in vivo* study, it is important that non-toxicity is assured. Therefore, a preliminary toxicity assessment was done on the synthesized metal-loaded nanoparticles.

2.2 Research Questions

The goals and objectives collectively narrow down the project to the following research questions:

> *1. Can the loading of metal ions with high atomic number into the nanoparticles be successful to a degree that can be expected to yield greater contrast, and can they be effectively utilized in distribution studies, potentially outperforming existing methods?*
>
> *2. What is the toxicity profile of the synthesized metal-loaded nanoparticles, and can the safety and efficacy of these loaded particles for in vivo applications be confirmed?*

3 Theory

3.1 Polymeric, Ion-enriched Nanoparticles

3.1.1 Enhanced Permeability and Retention Effect

Spago Nanomedical's technology platform is centered around two important properties; the chelating properties of the polymeric nanoparticles and the Enhanced Permeability and Retention effect (EPR effect). The former is responsible for the exceptional binding of functional metal ions and the latter is a physiological feature distinguishing healthy tissue from cancerous tissue.

The rapid growth of tumors require a large supply of oxygen and nutrients, causing the blood vessels surrounding tumors to undergo abnormal and rapid growth. This results in the capillary walls being more permeable to particles compared to vasculature in healthy tissue. Additionally, tumor tissue often has restricted lymphatic drainage, leading to a greater particle retention compared to non-tumor tissue [3]. The nanoparticle properties are designed to leverage this EPR effect, and is the reason for the efficacy of Spago Nanomedical's drugs. This has been confirmed clinically in patients with breast cancer as well as various preclinical cancer models [4] [5].

3.1.2 Structure

The nanoparticle consists of three main parts; a core, a primer and a coating, as seen in Figure 2.4. The central core is built up of bis-phosponate bis-organosilane precursor monomers as seen in Figure 3.1. The starting concentration of this monomer determines the resulting core size, allowing precise production of nanoparticle cores with the preferential size of 17 nm in diameter. Through a condensation polymerization, silanes link up with other silane monomers, into a network of siloxane (Si-O-Si) bonds, as seen in Figure 3.2.

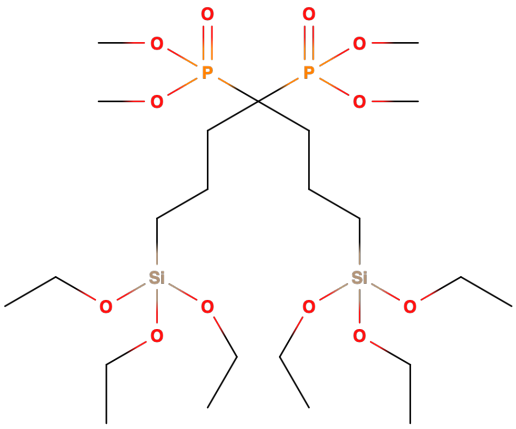

Fig. 3.1: Schematic illustration of bis-phosphonic acid monomer.

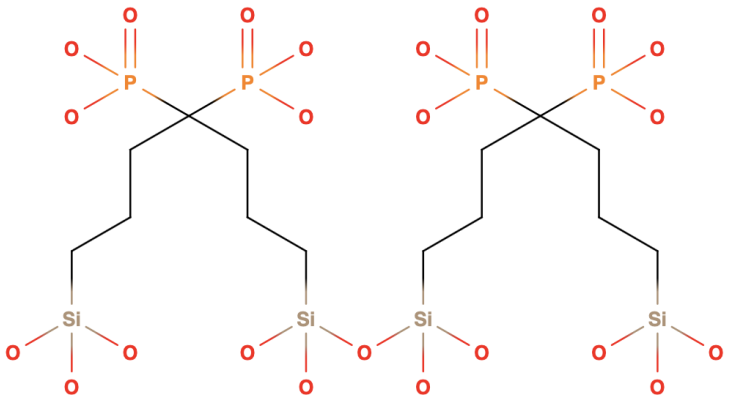

Fig. 3.2: Schematic illustration of bis-phosphonate bissilane precursor dimer.

At the same time, the methyl groups fall off the phosphonates, unmasking phosphonic acid groups, which enables binding of ions. The result of this polymerization is a mesh of chelating sites that have high affinity for metal ions as seen in Figure 3.3. The random nature of the polymerization creates randomly orientated phosphonic acid groups, resulting in all chelating sites having slightly different geometries.

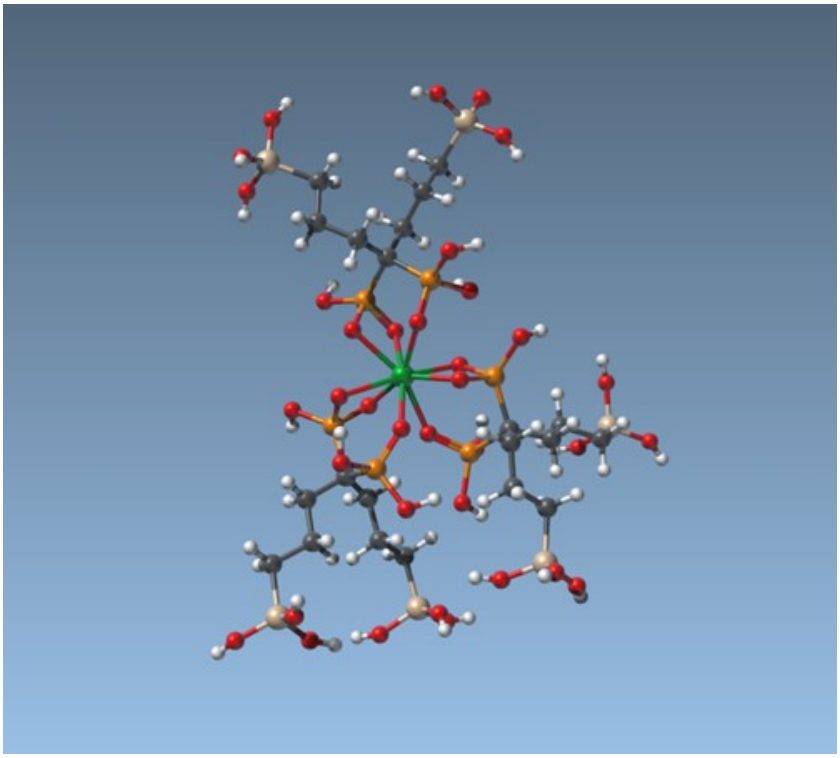

Fig. 3.3: Part of the core of a particle coordinating a lutetium ion. Lu^{3+}: green, P: orange, Si: beige, O: red, C: black, H: white. The silanols would in the real case be linked to other monomers to form an extended network.

Not all chelating sites have the optimal conditions to sufficiently bind an ion. The binding requires an adequate number of available bonds that are orientated in an appropriate way. Since the orientation of the core monomers is relatively random, each chelating site will exhibit different affinity for metal ions. Trivalent cations like Lu(III), likely preferentially form complexes with

eight or nine oxygen atoms. Consequently, the optimal chelating site would have six phosphonate groups, providing 9 oxygen atoms, as seen in Figure 3.3. In conclusion, the orientation of the monomers and the type of metal ion will determine how much of, and how well, the metal can bind [5].

After the synthesis of the core, a thin layer, called anchoring layer, is applied to improve binding to the final coating. The anchoring layer is derived from a bissilane, and builds a network polymer giving a better matching between the core and the outermost layer. The outer coating consists of many di-polyethylene glycol (PEG)-di silanes attached to the anchoring layer. The coating is dense and crucial for long-term stability and biocompatibility. It shields the particle from interactions with proteins and the immune system [6]. The final size of the nanoparticle is 27 nm in diameter. Figure 3.4 shows the complete nanoparticle and the chemical composition of each part.

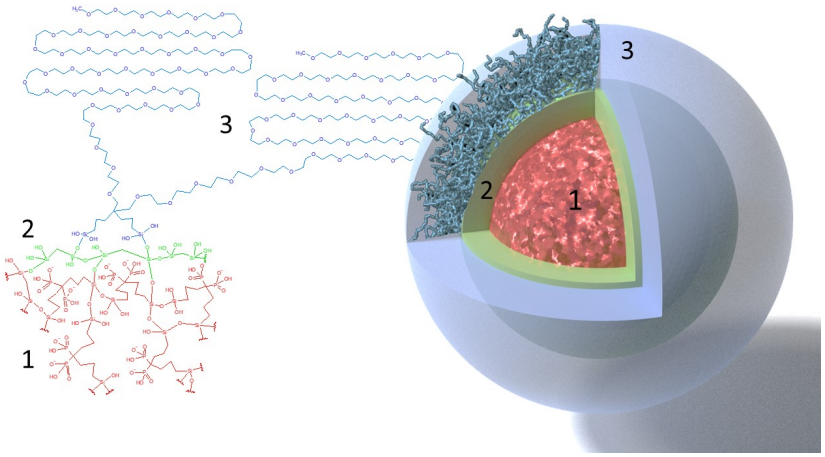

Fig. 3.4: Illustration of the complete nanoparticle and chemical composition of each part. (1) Core: red, (2) Anchoring layer: green and (3) PEG-coating: blue.

3.1.3 Metal-loading of the Nanoparticles

A batch of nanoparticles was produced in the spring of 2021 and is currently undergoing a long-term stability study. During the study, samples are stored at -70, -20, and 4 °C and have so far shown good stability of both the nanoparticle core and the added excipients. The batch is not loaded, meaning there are no added ions in the chelating sites of the core. The batch has a concentration of 60 mM of phosphorus. “Tox Batch” (SN201, JP01142E) is henceforward used as the name for this specific batch.

Left-over material from this study was used for the metal binding experiments in this thesis. The objective was to see if, and how much, metal can be bound in a process called ”loading”, without compromising the desired characteristics of the nanoparticle. To quantify the degree of metal incorporation into the particle, the metal content can be expressed as the phosphorous-to-metal ion ratio, $\frac{P}{M}$, where M is a metal ion. This is a useful measure since the metal ion chelation is dependent on the phosphonate groups. Moreover, considering the variability in the number of monomers present in nanoparticles, the phosphorous concentration emerges as the preferred

measurement in this investigation. Nanoparticles from previous loading experiments showed an unexpectedly high amount of metal, with $\frac{P}{M}$ ratios below 2. The theoretical complex discussed in 3.1.2 would result in a ratio of 3, since each metal ion preferably binds to 9 oxygen and each phosphonate can provide 3 oxygen. The random orientation of the phosphonates is expected to result in a lower ratio, however, the observed number is still surprisingly low. The current theory of how this is possible is that the increase in pH during the ion-chelation process, could cause surface-associated, dissolved metal or aggregates to get drawn into pockets in the particle due to the relative increase in negative charge of the phosphonates. The change in pH could potentially also lead to aggregation and/or precipitation on the surface of the nanoparticles, leading to possible toxic effects and a decrease in biocompatibility, as well as a significant decrease in $\frac{P}{M}$ ratio.

To test the aforementioned hypothesis, two batches were prepared using two different protocols. One where the solution was pH adjusted before filtration and washing, called ”Basic Protocol”, referring to the pH being brought up before the spin filtration, and one where the pH adjustment was performed after filtration and washing called ”Acidic Protocol”, due to the relatively high acidity during spin filtration. Note that the high amount of metal loading is not necessarily negative, just surprising, and a curiosity to investigate.

The selection of metal ion candidates was based on several desired properties. Firstly, the metal ion should possess 3+ or 4+ charge, since this is essential for the high binding affinity to the nanoparticle core. Secondly, the chosen candidates must demonstrate relatively low toxicity and non-radioactivity, eliminating all elements heavier than bismuth and some known toxic elements. Lastly, as the goal is to use the particles as contrast agents in *in vivo* imaging, the metal ions should have a high atomic number. The aforementioned criteria collectively narrow down the pool of candidates. Excluding some extremely rare and thereby impractically costly elements, this leaves bismuth (Bi^{3+}), gadolinium (Gd^{3+}), hafnium (Hf^{4+}) and lutetium (Lu^{3+}) as potential candidates.

3.2 Characterization

Size determination can be performed to ensure that the particles are intact and of the expected dimensions. This process can also detect the existence of aggregated particles or other byproducts such as metal oxide aggregates. Size Exclusion Chromatography (SEC) and Dynamic Light Scattering (DLS) are two techniques utilized for size determination. Both methods require samples within certain concentration ranges to give reliable results. This makes elemental characterization and quantification a prerequisite. To provide this information, Inductively Coupled Plasma Optical Emission Spectrometry (ICP-OES) is used.

3.2.1 Inductively Coupled Plasma Optical Emission Spectrometry

Inductively Coupled Plasma Optical Emission Spectrometry, is an analytical technique for detection and quantification of elements, which can be used to calculate metal incorporation (the $\frac{P}{M}$)

and concentration. The technique uses ionized gas, or plasma, electromagnetically heated to very high temperatures via an induction coil. The sample is introduced to this plasma as an aerosol, and atoms are excited, meaning the outer electrons jump to an orbital of higher energy. The electrons only stay here briefly (around 10^{-8} s) before they relax back to a lower energy orbital, emitting electromagnetic radiation with a wavelength corresponding to the difference in energy between the orbitals. Chemical bonds are dissociated at the temperature of the plasma, which makes the emitted radiation independent of the chemical structure of the sample, and purely dependent on the specific emission frequency of the elements. The heating leads to emission of light in discrete lines, which can be separated according to wavelength by diffractive optics and subsequently used for elemental identification. Quantification of elements uses the intensity of the emitted light from the sample, and is based on the prerequisite that the intensity is proportional to the concentration. However, this concentration-intensity relationship depends on many parameters, and calibration can be a challenge [7].

In practice, ICP-OES operates by configuring the instrument to detect a specific wavelength corresponding to the desired target element. The intensity of this wavelength is compared to a standard curve. Obtaining the standard curve is done by analyzing a serial dilution of the target element with known concentration. This dilution can be done by a 3/3/3/2 serial dilution of a known standard for each element. The diluent employed at Spago Nanomedical is water mixed with 1% HNO3 + 5% HCl + 1% Triton X-100 (”1+5+D”). Triton X-100 is a detergent used to obtain a linear response from the phosphorous in Spago’s nanoparticles. It is not completely known why, but without detergent the ICP response is non-linear and unreliable. The current theory is that detergent reduces the diameter of the droplets in the ICP, thereby enhancing pyrolysis efficiency in the torch. Conversely, larger droplets may not undergo proper evaporation, resulting in unpredictable responses. Since the emitted intensity will be proportional to the concentration, an intensity-concentration calibration curve can be constructed. The wavelength selected for detection should correspond to the emission signals from the atoms of interest. Most instruments allow for the selection of multiple wavelengths enabling detection of multiple elements simultaneously, presenting a significant advantage over other methods [7]. ICP works by interpolation with the standard curve. Consequently, samples must be appropriately diluted to ensure they fall within the intensity range of the standard curve.

3.2.2 Dynamic Light Scattering

Dynamic Light Scattering (DLS) is a technique used to measure the hydrodynamic volume of particles and macromolecules in a solution. The working principle of the technique is to measure the Brownian motion of the sample particles and use this information to estimate the diffusion coefficient. The diffusion coefficient can subsequently be used to calculate the hydrodynamic diameter of the particles. Hydrodynamic diameter is the diameter of a hypothetical sphere that diffuses at the same rate as the particle under investigation. The Stokes-Einstein equation 3.1 describes the relationship between size and diffusion.

$$D_\tau = \frac{2k_BT}{6\pi\eta D_h} \longleftrightarrow D_h = \frac{2k_BT}{6\pi\eta D_\tau} \tag{3.1}$$

where D_τ is the diffusion coefficient, k_B is the Boltzmann coefficient, T is the temperature, η is the viscosity of the surrounding medium, and R_h is the hydrodynamic diameter. From equation 3.1 it is deduced that larger particles diffuse slower than smaller particles [8].

In the instrument, a laser beam is passed through the sample, where the particles are undergoing Brownian motion, and the intensity fluctuations of light scattered at an angle to the incident light are measured. The working principle of DLS is schematically shown in Figure 3.5. This information can be analyzed to estimate the diffusion coefficient and calculate the particle size using equation 3.1 [8].

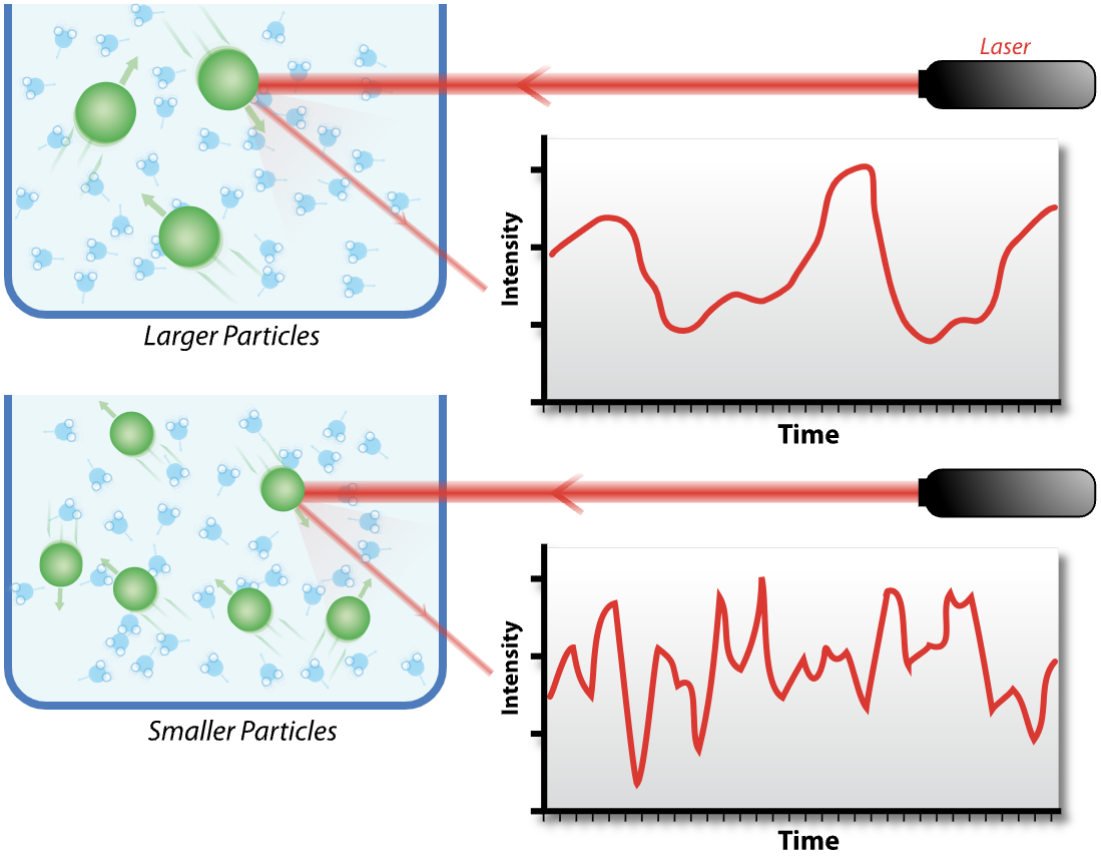

Fig. 3.5: Schematic image of how DLS works. (By Mike Jones - Own work, CC BY-SA 3.0, https://commons.wikimedia.org/w/index.php?curid=10502233)

Dynamic Light Scattering is a rapid, versatile and relatively dependable approach for mean size measurements, however, size distribution is not reliably measured. DLS is also potentially sensitive to changes in temperature and viscosity of the medium, as well as any aggregates in the sample [9]. Because of the low resolution and the inadequate determination of size distribution, DLS is often complemented with Size Exclusion Chromatography (SEC). SEC is more sensitive to size distribution, but demands more time and labor. Furthermore, determining absolute size requires comparison to known standards.

3.2.3 Size Exclusion Chromatography

Size Exclusion Chromatography (SEC) is a type of high-performance liquid chromatography (HPLC), which is a group of techniques in analytical chemistry used for identifying, separating and quantifying semi- and non-volatile compounds in liquid samples [10]. SEC is a general name encompassing the process of separating particles according to size. With the help of a solvent, the sample solution is carried through a column, which is packed with a porous material. The process of particle size separation occurs as a consequence of the relationship between retention time and the hydrodynamic volume of the sample. This correlation arises from the fact that smaller molecules possess a comparatively larger accessible volume within the porous stationary phase, resulting in extended retention times, see Figure 3.6.

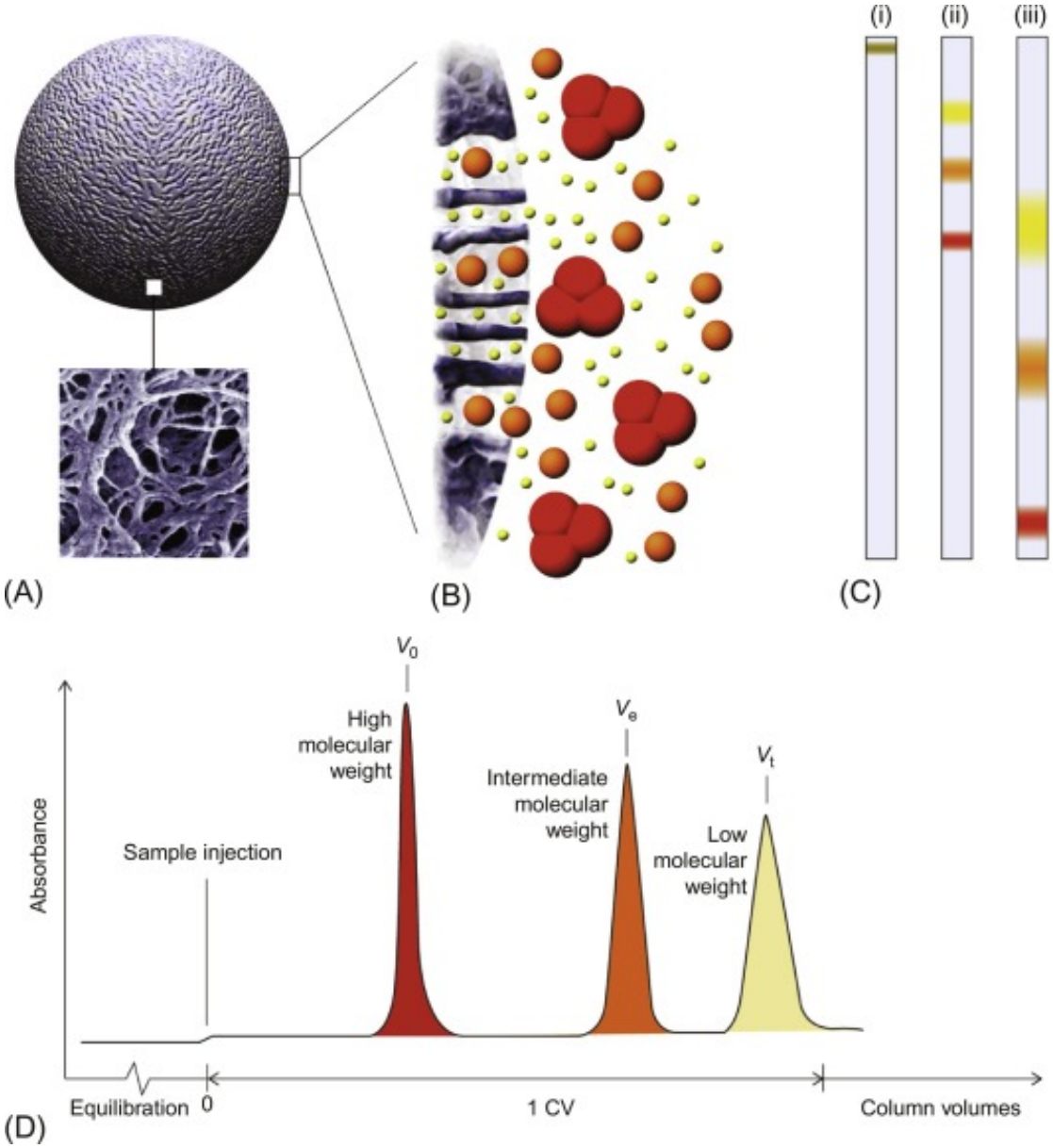

Fig. 3.6: Schematic image of Size Exclusion Chromatography. [11]

In SEC the material in the column is often a highly cross-linked spherical polystyrene/divinyl benzene, which creates the porous matrix with a specific pore diameter [12]. This immobile material in the column is referred to as stationary phase, while the solvent which carries the

sample is called mobile phase. In contrast to other techniques, the separation in SEC is essentially mechanical, whereas other forms of chromatography are based on chemical interactions between the stationary phase and the mobile phase to separate molecules [13]. To detect the eluted molecules, an Evaporative Light-Scattering Detector (ELSD) can be used. As the name suggests, ELSD works by heating the eluate to selectively evaporate the solvent and retain the analyte for detection. To exclusively evaporate the solvent, the analytes have to be less volatile than the mobile phase solvent. The retained analytes then pass through a laser beam. The particles scatter the light and the intensity of scattered light is detected by a photo diode to determine quantity. The time of detection gives the size of the detected particle due to the aforementioned relationship between retention time and size [14]. The hydrodynamic diameter of the samples can finally be calculated by comparing the retention time to a set of standard molecules with known retention time and hydrodynamic volume. Beyond size calculations, the standard molecules can be used to analyse long-term shift in size. If the material degrades over time, new peaks corresponding to the impurities will emerge. Additionally, the measured SEC peaks of the particles will start shifting in relation to the well defined standards.

Ultraviolet detectors are also often used in HPLC for their ease of use and sensitivity. UV detectors work by measuring the amount of absorbed light by the eluted analyte, through which size and relative quantity is determined [15]. However, UV detectors can only detect samples with chromophores or fluorophores, making them less versatile than ELSD detectors, which response is based on the mass of the particle and does not depend on the optical characteristics of the analyte.

3.3 Transmission Electron Microscopy Imaging

Transmission Electron Microscopy (TEM) is a type of microscopy that, unlike light microscopes, utilizes electrons. Transmission Electron Microscopy is a powerful tool that allows for material study at the atomic level, offering the highest resolution and magnification of any microscopy technique. TEM works by accelerating electrons in a vacuum tube, forming a beam that is focused on the sample. The electron beam is transmitted through the sample and interacts with electrons and protons in it, which causes different forms of scattering. Depending on the sample and what you aim to measure, different types of scattered electrons are used. Detectors are generally set up to measure the desired form of scattering by selectively absorbing electrons from a specific angle or direction. The intensity of electrons measured by the detector is finally converted to an image [16].

The so-called de Broglie wavelength relates a particle's wavelength λ to its momentum p through Planck's constant h as shown in equation 3.2 [16].

$$\lambda = \frac{h}{p} \tag{3.2}$$

By some substitutions, this equation can be rewritten as follows:

$$\lambda = \frac{h}{\sqrt{2m_0 eV}} \tag{3.3}$$

where m_0 = the rest mass of an electron, e = the charge of an electron, and V = the acceleration voltage of the microscope. Equation 3.3 provides an estimate that neglects relativistic effects. Nevertheless it shows that as acceleration voltage of the microscope increases, the wavelength of the electrons decrease, thereby enabling higher resolution. While this might suggest that greater acceleration voltage yields superior outcomes, it also results in a smaller elastic scattering cross section, thereby lowering the probability of elastic scattering, and consequently worse contrast [17]. As a consequence, achieving optimal image quality of certain samples requires finding balance between resolution and contrast. This is particularly true for non-crystalline samples lacking sufficient density, such as Tox batch nanoparticles.

Various types of TEM exist, each representing variations of Conventional Transmission Electron Microscopy (CTEM). Among these, Scanning Transmission Electron Microscopy (STEM) stands out as one of the most common. STEM closely resembles CTEM, differing primarily in its utilization of scanning techniques for image acquisition. While CTEM illuminates a substantial portion of the sample, STEM employs a focused beam, known as a probe, which scans across the specimen to construct an image. STEM also differs from TEM in how electrons are measured. While TEM employs an aperture for electron selection, STEM employs detectors for direct measurement of target electrons. A predominant STEM detector is the High Angle Annular Dark Field detector (HAADF), designed to capture electrons that have scattered at high angles. HAADF detectors primarily captures elastically scattered electrons, arising from interactions with atomic nuclei through Coulombic forces. Consequently, HAADF exclusively yields contrast related to the atomic number Z [16, 18, 19].

Aside from obtaining images, Transmission Electron Microscopes can be used as an instrument for chemical analysis in so called Analytical Electron Microscopy (AEM). This is done by utilizing X-ray Energy-Dispersive Spectrometry (XEDS) or Electron Energy-Loss Spectrometry (EELS), and allows analysis of elemental composition, band structure, bonding state and more. XEDS can be used in parallel with other TEM detectors and works by measuring photons (x-rays) instead of electrons. When the sample is exposed to the electron beam, some electrons in the sample absorb sufficient energy to be ejected from their orbitals. Subsequently, electrons from higher energy orbitals relax to fill these vacancies. In this relaxation process, a photon is emitted with an energy equivalent to the difference between the two orbitals. This difference in energy is specific to each element and can be used for analysis of chemical composition. Electron energy-loss spectrometry also works by measuring energies, but instead of photons it utilizes inelastically scattered electrons, i.e. electrons that have lost energy, to obtain a spectrum of energies that can be used for sample analysis [16].

Transmission electron microscopy is an extremely powerful method of analysis, but it has limitations. First of all, since the electron beam is ionizing radiation, samples can be damaged during examination. This is particularly true for polymers and organic materials, which is precisely what this study aims to investigate. Destruction of the sample is not necessarily a problem, but it is important to keep in mind as you analyse the results since the beam potentially interacts with, and changes, the sample. Another problem is that interpretation of the image can be challenging. TEM presents us with a two-dimensional image of a three-dimensional object, potentially resulting

in misleading representations of reality. Additionally, TEM requires samples that interact with the electron beam and cause scattering, which in general means that crystallinity or high atomic number is essential for high contrast and resolution [16].

3.4 Cytotoxicity Assessment

Cytotoxicity assessment is highly relevant to investigate the possibility of using the metal-loaded nanoparticles *in vivo* or other medical contexts. The level of cytotoxicity and biocompatibility can be established by exposing *in vitro* cells to a serial dilution of the test item. Exposure to increasing concentrations will indicate toxicity by a progressive reduction in the viability of the cell population. The choice of cell line depends on the aim of the study. RAW 264.7 is a well established cell line derived from mice that is regarded as an appropriate model for human macrophages [20]. RAW 264.7 cells are commonly used in cytotoxicity assessments due to their relatively robust nature and ability to phagocytose pathogens. Utilizing an established and well characterized cell line also provides consistent and reproducible results. To obtain reliable and comparable data, and ensure cells are not dying due to procedural errors, controls are used. An unexposed control referred to as negative control is used to compare relative cytotoxicity. This control remains unexposed to the test item and should hence exhibit minimal to no decrease in cellular population. Conversely, a positive control is subjected to a cytotoxic agent like Sodium Dodecyl Sulfate (SDS), resulting in eradication of the entire population. SDS is a detergent which kills cells by denaturing proteins and disrupting the lipid bilayer of the cell membranes [21, 22]. This control group primarily acts as a zero reference in the viability assessment. In addition to the controls, reference samples may be used to facilitate comparative analysis between samples. As this study aims to determine toxicity of metal-ion enriched nanoparticles, it is logical to compare the results with those derived from solutions containing the equivalent concentration of metal, devoid of nanoparticles.

A common viability assay uses CellTiter-Blue and UV-fluorescence. CellTiter-Blue is based on the ability of living cells to convert a redox dye into a fluorescent product. Conversely, non-viable cells are unable to break down the dye, and hence no fluorescence occurs. CellTiter-Blue emits light at a wavelength of 590 nm. By measuring the intensity of light emitted at this wavelength and comparing to the positive and negative controls, the relative viability of the populations can be deduced [23].

4 Methods

4.1 Experimental Setup

4.1.1 Metal-loading of the Nanoparticle

The salts chosen for each respective metal was bismuth-acetate, gadolinium chloride hexahydrate, hafnium chloride, and lutetium chloride hexahydrate. Our objective was to achieve a phosphorus to metal-ion ratio of 2:1. This decision was based on previous experiments at Spago that indicated reliable loading to this extent. Surpassing this ratio could theoretically lead to undesirable aggregation and/or metal oxide formation. The mass of metal salt to achieve this ratio was calculated and added to a 4 mL vial, together with 1 mL Tox Batch (60 mM P). A small magnet was added to each vial and the samples were incubated at room temperature overnight. After the incubation, the samples were centrifuged at 13 400 rpm, 12 000 g for 10 minutes. Avoiding pelleted material, the samples were transferred to new 4 mL vials, before being diluted to a total volume of 2.0 mL with Milli-Q water (MQ water). Two protocols with slight differences were used from this point.

Following the ”basic protocol”, the pH of the samples were adjusted to just above 7.0 using Tris-HCl (0.1 M, pH 8) and a Micro-Pro-ISM pH-electrode for measurement. The samples were spin filtered to remove surplus of metal compound using an Amicon Ultra-4 filter with a 100 000 molecular weight (MW) cut-off. The permeate was discarded while the retentate was diluted by a factor of 11 with MQ water. This was repeated three times, acquiring a dilution factor of over 1300. To provoke weakly associated metal ions to dissociate, samples were diluted by a factor 11 with 10 mM $CaCl_2$ solution and incubated for one hour at room temperature. The spin filtration was conducted three additional times to filter out unwanted compounds and surplus $CaCl_2$. After the final filtration of the basic lutetium samples, a ”gel-like” consistency was observed, indicating a very high concentration of nanoparticles. This consistency was most likely caused by increased interaction between the particles, in particular when the concentration exceeds a volume fraction of 15-20 % [1]. 1 mL of MQ water was added to reduce the viscosity. All samples were transferred to 4 mL vials and the filters were washed with MQ water to extract any left-over particles. The final volume was approximately 1 mL, with the exception of the basic lutetium sample at approximately 2 mL.

Following the acidic protocol, samples were prepared using a similar procedure as in the basic protocol, with the exception of pH adjustment being executed between the spin filtration and $CaCl_2$ provocation steps. The difference in materials employed was the utilization of Tris-Base 0.5 M instead of Tris-HCl for the pH adjustment, chosen due to the lower acidity of the samples. The samples were now finished and ready for analysis, see Figure 4.1.

Two additional samples where prepared specifically for TEM imaging purposes. These where designed to have maximized loading in order to achieve high contrast in TEM. Consequently,

both samples where prepared using the basic protocol and loaded with the heaviest element, bismuth. The target ratios were 1:1 and 0.5:1 respectively.

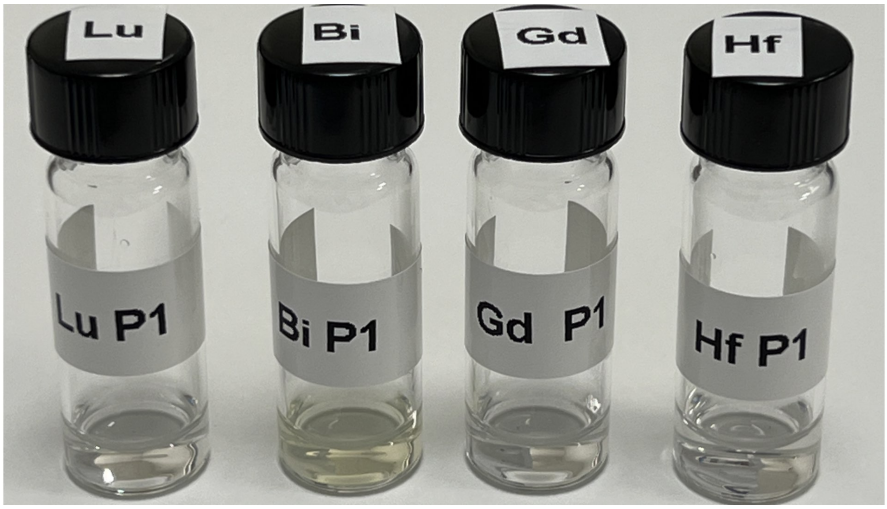

Fig. 4.1: Finalized samples from protocol 1. Note the yellow tint of the bismuth sample, suggesting a difference from the other samples.

Table 4.1: Table over all sample names and the protocol used to produce them.

Samples		
Sample Name	Description	Protocol Used
Acidic bismuth	Lutetium, 1 mL Batch	Acidic Protocol
Acidic gadolinium	Gadolinium, 1 mL Batch	
Acidic hafnium	Hafnium, 1 mL Batch	
Acidic lutetium	Lutetium, 1 mL Batch	
Basic bismuth	Lutetium, 1 mL Batch	Basic Protocol
Basic gadolinium	Gadolinium, 1 mL Batch	
Basic hafnium	Hafnium, 1 mL Batch	
Basic lutetium	Lutetium, 1 mL Batch	
Bi 0.5	Bismuth, TEM Batch, 0.5:1 Ratio	Basic Protocol
Bi 1:1	Bismuth, TEM Batch, 1:1 Ratio	

4.2 Analytical Methods

4.2.1 Inductive Coupled Plasma Optical Emission Spectrometry

All samples were analyzed using ICP with the parameters shown in Table A.1. ICP analysis requires a standard curve of known concentrations. Thus, a standard solution needed to be prepared for each element that would be analyzed. This was accomplished by a 3/3/3/2 serial dilution of a known standard for each element. The diluent employed was water mixed with 1% HNO3 + 5% HCl + 1% Triton X-100 (”1+5+D”). The serial dilution protocol can be seen in Table 4.2 and the resulting concentrations for each dilution A-E can be seen in Table A.2. The standards were then measured using ICP to acquire an intensity-concentration proportionality curve for each element, an example can be seen in Figure 4.2.

Table 4.2: Table over standards used for ICP elemental analysis with volume for stock standard

Standards for ICP — Volumes Used			
Dilution	Dilution Factor	Volume of standard (mL)	Volume of 1+5+D
A	1	50	0
B	3	16.7	33.3
C	9	5.56	44.44
D	27	1.85	48.15
E	54	0.62	49.38

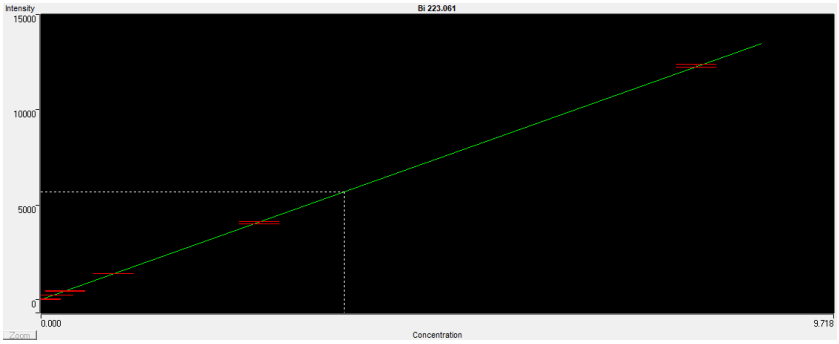

Fig. 4.2: Graph showing the linear proportionality between intensity and concentration for Bi wavelength 223.061 nm. The red lines indicate the standards from which the linear curve is determined. The dotted lines indicate the concentration and intensity of bismuth prepared using the basic protocol, diluted by a factor 2800.

After the standard curve was acquired, the samples could be analyzed. Samples were diluted to end up within the concentration interval of the standard curve. This dilution was based on educated guesses, resulting in some trial and error to achieve concentrations within the specified range. The final dilutions are displayed in Table 4.3. For higher accuracy, duplicates of each sample was analysed and an average was calculated. An example of the resulting intensity curve from ICP analysis can be seen in Figure 4.3. The intensity from these measurements were then interpolated against the standard curve for each corresponding element, yielding the elemental concentrations.

H

Table 4.3: Final dilution factors used in ICP.

Sample	Bi P1	Bi P2	Gd P1	Gd P2	Hf P1	Hf P2	Lu P1	Lu P2
Final dilution factors	972.9	2442.2	1024.2	832.1	1039.1	976.9	1024.3	7826.0

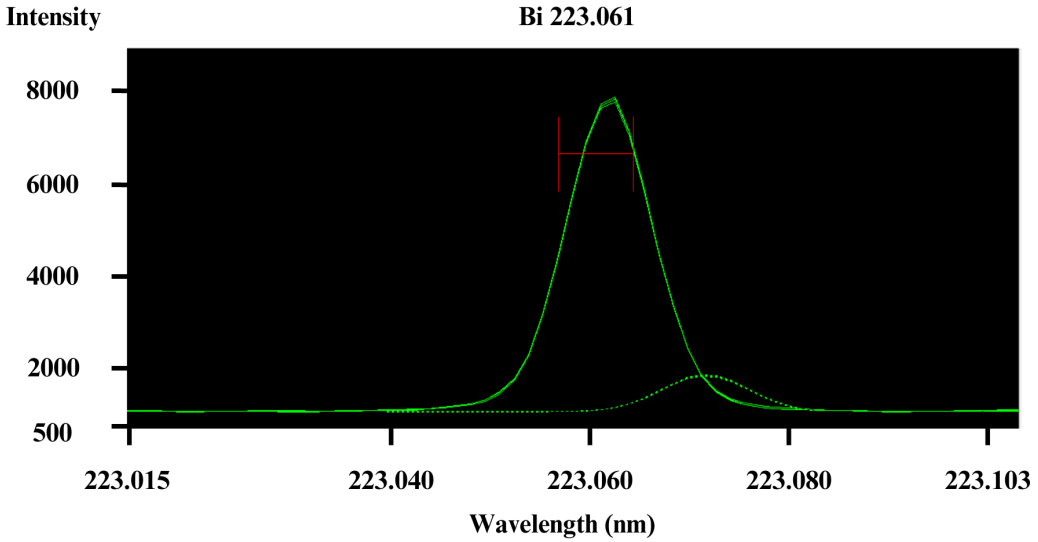

Fig. 4.3: Intensity spectrum of bismuth prepared with basic protocol. Red lines indicate the specific wavelength for bismuth. The dotted line is the baseline calculated by the ICP program.

4.2.2 Dynamic Light Scattering

The original Tox Batch nanoparticles were used as reference since they have a known size and phosphorus concentration. The unloaded Tox Batch nanoparticles were diluted to a concentration of 6 mM P and a total volume of 500 µL. The metal loaded samples were prepared by calculating the volume needed to achieve the same phosphorus concentration, and hence particle concentration, as the Tox Batch reference. The volumes needed are given by equation 4.1.

$$V_{sample} = \frac{C_{Ref} V_{Ref}}{C_{sample}} = \frac{6\ mM \cdot 500\ \mu L}{C_{sample}} \tag{4.1}$$

Where V_{sample} is the desired sample volume, C_{ref} is the concentration of phosphorus in the reference, V_{ref} is the total volume of the reference and C_{sample} is the concentration of phosphorus in the sample undergoing analysis. The concentration of the samples were obtained from the previously performed ICP analysis. The calculated sample volumes were diluted to a total volume of 500 µL, added to DLS cuvettes and analyzed using the settings seen in Table A.3. The parameters were previously established empirically by Spago, demonstrating reliable measurements for the nanoparticles using this particular instrument.

4.2.3 Size Exclusion Chromatography

The mobile phase used for the SEC measurements was 50 mM aqueous ammonium acetate [NH4CH;C02] + 10 % v/v acetonitrile. First, a set of standards were prepared. Bovine Serum Albumin (BSA), thyroglobulin, cowpea mosaic virus (CPMV), polyethylene-oxide 1000 kDa (PEO-1000k) and polyethylene-oxide 165 kDa (PEO-165k) were diluted in ammonium acetate buffer, i.e. the mobile phase but without acetonitrile. Each of these standard molecules demonstrates dimensions closely resembling those of the nanoparticles, with particular emphasis on CPMV, possessing a diameter of approximately 28 nm, which aligns nearly identically with the dimensions of the nanoparticles [2]. Neither PEO-1000k nor PEO-165k possess sizes suitable for direct size comparison. However, due to their exceptional stability, they serve as reliable benchmarks to detect any drift in nanoparticle size over time, as well as broadening of the peaks.

The standard solutions were then diluted again with mobile phase according to Table 4.4, while the samples were prepared to have the concentrations in Table 4.5. The five standards were then analysed together with the samples and used for the calibration curve. The injection sequence was a predetermined HPLC method for the nanoparticle, following this sequence; blank sample (i.e. mobile phase), BSA, thyroglobulin, CPMV, polymer standards and lastly the nanoparticle samples. Blank samples were injected between each injection to rinse the previous analyte. The method used the settings and properties in Table A.4.

Table 4.4: Concentrations of the prepared SEC standards.

Standard	Concentration, Dilution 1 (mg/mL)	Concentration, Dilution 2 (mg/mL)
CPMV	1.00	CPMV injected directly.
PEO 1000k	5.14	1.03
PEO 165k	6.10	1.22
Thyroglobulin	4.40	1.32
BSA	4.30	0.86

Table 4.5: Dilution factors and final concentration of samples in SEC.

Sample	Dilution factor in mobile phase	Concentration of P after dilution (mM)
Tox batch reference	3	20.00
Bi Acidic	2	19.5
Bi Basic	6	19.17
Gd Acidic	2	17.55
Gd Basic	2	24.05
Hf Acidic	2	17.00
Hf Basic	2	19.20
Lu Acidic	2	16.30
Lu Basic	2	22.15

4.2.4 Transmission Electron Microscopy Imaging

The nanoparticles analyzed in the first TEM-session were the basic lutetium batch and basic hafnium batch. The samples had to be diluted to get an optimal particle density on the TEM grid. Previous imaging performed with the nanoparticle indicated that diluting to a TEM grid coverage of 400% yielded desirable particle density. In other words, dilution to a concentration resulting in

the projected area of all particles covering the TEM grid fourfold. This was roughly calculated utilizing the known concentrations of phosphorus as follows:

$$C = \frac{n}{V} = \frac{N_P}{N_A V} = \frac{A_{grid}}{A_{particle}} \cdot \frac{4 \cdot N_{P/particle}}{N_A V} \tag{4.2}$$

where C is the desired concentration of phosphorus, n is the amount of phosphorus, V is the sample volume, N_P is the number of phosphorus atoms required for a fourfold coverage, N_A is the Avogadro constant and $N_P/particle$ is the number of phosphorus atoms per nanoparticle. The grid used was 3 mm in diameter, the particle diameter was approximated to 30 nm in diameter, the volume was 6 µL and the number of phosphorus per nanoparticle was 16000. This resulted in a desired concentration of 177 µM. All TEM samples were diluted to these concentration using ammonium bicarbonate, as it prevents the particles from clustering and sublimates into non-problematic gases, i.e. carbon dioxide, water and ammonia, in the vacuum of the TEM. The volume of dilute added to 5 µL of sample can be seen in Table 4.6. The samples were diluted by a factor 20 and two new grids where prepared according to the previously described procedure. This resulted in a concentration of 8.85 µM P for both the Lu and Hf sample.

Table 4.6: Volume of ammonium bicarbonate to 5 µL of sample, resulting in a final concentration of 177 µM.

Sample	Volume of Ammonium Bicarbonate (µL)
Lu P2	1245
Hf P2	1080
Bi 0.5	532
Bi 1.0	568

The grids used for TEM was a copper grid with lacey carbon film. The grids where cleaned in a Quorum Glocube glow discharger at 20 mA for 30 seconds. The grids were then extracted from the machine and placed on a sheet of filter paper. Within 10 seconds of plasma treatment, 6 µL of the prepared samples were pipetted onto the grids and excess solvent was drained off by capillary effects by the filter paper. The samples were left to absorb onto the grid for 1 minute. Once complete, the grids were inserted into a 300 kV JEOL Analytical HR-TEM 3000F. The samples were analyzed using Bright field conventional TEM with and without apertures to achieve optimal contrast. XEDS was also performed on a region with a high concentration of particles, allowing elementary analysis. Dark field STEM was employed, using a High Angle Angular DF detector at 79-210 mrad. The higher sample concentration was too high rendering it impractical to obtain images of individual particles, see image 4.5. CTEM and STEM was repeated for the two samples with 1/20 concentration using the same procedure.

The images obtained from the initial TEM session revealed intriguing findings; however, the high acceleration voltage led to insufficient contrast. This motivated the use of a lower acceleration voltage during the subsequent session. For this session, the two new samples labeled Bi 0.5 and Bi 1 discussed in 4.1.1, were prepared and analyzed using the 200 kV JEOL Cryo-TEM 2200FS at an acceleration voltage of 120 kV. The freshly prepared samples were diluted to a concentration of 8.85 µM P using ammonium bicarbonate and subsequently applied to the grids following the previously outlined procedure. Thereafter, the samples were imaged utilizing various energy

filters and apertures.

4.2.5 Cytotoxicity Assessment

The cell toxicity assessment required a larger sample volume than was available, so an additional 10 mL batch of all samples were prepared using the protocol described in 4.1.1. Cell toxicity was tested by exposing cultured RAW 264.7 cells to serial dilutions of the samples. The dilutions with highest concentration were determined to 2 mM due to previous studies indicating cytotoxicity around this value for gadolinium [3, 4]. Since the cell cultures need a substantial amount of cell medium, the samples had to be at least 20 mM before dilution. Most samples were too dilute and were thus concentrated by applying a steady stream of nitrogen gas. Unlike for example spin filtration, utilizing nitrogen gas to evaporate the water ensures there is no contamination and no loss of sample. In addition to the nanoparticle samples, four control samples were prepared. The controls were prepared by diluting the same metal salts as in the loading phase, with 0.9% NaCl solution. All samples were diluted according to Table 4.7.

Table 4.7: Table of concentration and final volume after serial dilution.

Dilution name	Sample concentration (mM)	Total volume prepared (µL)
Dil 1	4	700
Dil 2	3	550
Dil 3	2	700
Dil 4	1.5	350
Dil 5	1	700
Dil 6	0.5	650
Dil 7	0.25	550
Dil 8	0.125	350

RAW264.7 cells were seeded in 96-well plates by adding 200 µL of cell solution at a concentration of $2.5 \cdot 10^5$ cells/mL to each well, resulting in 50 000 cells/well, see Figure 4.4 for seeding layout. The cell medium used was RPMI 1640 + 10% fetal bovine serum and Na-pyruvate. Cells were incubated for 24 hours in 37 °C and 5% CO_2. Serial dilution of the samples were performed according to Table 4.7 and 10% (w/v) SDS + medium solution was prepared. The media was removed by inversion and 50 µL of new medium was added to each well. An additional 50 µL of test item or media was added to the wells according to layout Figure 4.4. The sixth column was not subjected to any test item, acting as an uninfluenced control. Similarly, the eleventh column was not subjected to any sample since the cells in these wells were expected to die regardless. Plates were incubated at 37 °C, 5% CO_2 for 22 hours. After incubation, 20 µL of 10% SDS was added to the positive control, and 20 µL CellTiter-Blue was added to each well. Plates were incubated for an additional two hours at 37 °C, 5% CO_2. Figure 4.5 depicts one of the plates exposed to basic lutetium particles, after the final incubation. At the end of the incubation period, the fluorescence of 565/595 nm was measured using a SpectraMax i3x Multi-Mode Microplate Reader.

All Np	Cell / No Cell	1	2	3	4	5	6	7	8	9	10	11	12
A													
B	No Cell		Dil 1	Dil 2	Dil 3	Dil 4	Dil 5	RPMI	Dil 6	Dil 7	Dil 8	RPMI + Triton X-100	
C			Dil 1	Dil 2	Dil 3	Dil 4	Dil 5	RPMI	Dil 6	Dil 7	Dil 8	RPMI + Triton X-100	
D	Cell		Dil 1	Dil 2	Dil 3	Dil 4	Dil 5	RPMI	Dil 6	Dil 7	Dil 8	RPMI + Triton X-100	
E			Dil 1	Dil 2	Dil 3	Dil 4	Dil 5	RPMI	Dil 6	Dil 7	Dil 8	RPMI + Triton X-100	
F			Dil 1	Dil 2	Dil 3	Dil 4	Dil 5	RPMI	Dil 6	Dil 7	Dil 8	RPMI + Triton X-100	
G			Dil 1	Dil 2	Dil 3	Dil 4	Dil 5	RPMI	Dil 6	Dil 7	Dil 8	RPMI + Triton X-100	
H													

Fig. 4.4: Schematic dilution layout of the 96-well plates.

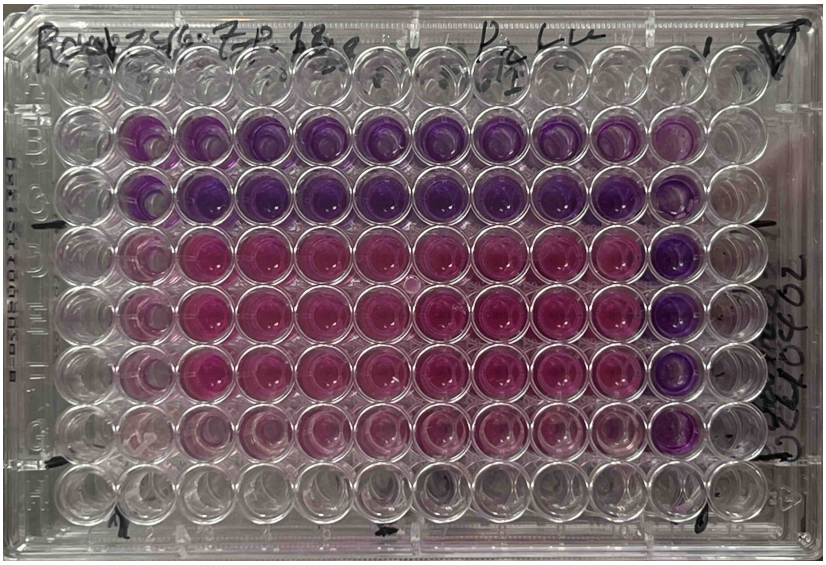

Fig. 4.5: Image depicts one of the microplates after addition of basic lutetium sample, CellTiter-Blue and a final incubation. Note that the CellTiter-Blue is related to UV-fluorescence and not the color of the solution in the wells. The color is primarily affected by the degree of dilution.

5 Results and Discussion

5.1 Characterization of Nanoparticles

The characterization of the nanoparticles is a critical step in understanding their properties and assessing their potential use. This section presents a comprehensive analysis of the particles synthesized in our study, focusing on the degree of metal loading, their size distribution, and morphology. Through analysis using ICP-OES, we quantitatively determine the incorporation of metal ions into the nanoparticles, providing insights into their composition. Subsequently, size and distribution analysis through DLS and SEC provides the dimensional characteristics of the nanoparticles, crucial for assessing if the particles are intact and free from aggregates. Additionally, morphology examination through TEM imaging provides visual information of the structural integrity and surface features of the particles, as well as providing a method to confirm the size of the particle core. Finally, cytotoxicity evaluation provides valuable insights into the potential toxic effects of the nanoparticles. Together, these analyses offer a comprehensive characterization of the synthesized nanoparticles, presenting evidence of the success of the metal-loading protocol and their potential in upcoming *in vivo* experiments.

5.1.1 Metal Loading Analysis from Inductively Coupled Plasma Optical Emission Spectrometry

The elemental concentrations and composition of the particles were determined using ICP-OES analysis. Figure 5.1 shows the ratio of phosphorus to metal for all samples. Notably, there is significant variability in the concentrations of phosphorus and metal among the samples. This variability underscores the relevance of the P/M ratio as a metric for evaluating elemental composition and metal incorporation. Given that the concentrations of phosphorus and metal exhibit a linear and interdependent relationship, the P/M ratio serves as a more reliable measure for these analyses. A comparative analysis of the acidic and basic protocols reveals that the acidic protocol generally yields a higher P/M ratio, except in the case of bismuth.

The higher ratio for the acidic protocol was expected and can be attributed to when the pH adjustment occurred. As discussed in 2.1.3, in the basic protocol the pH adjustment preceded filtration and washing, resulting in a presence of free metal ions in the solution. As the pH levels rise, the phosphonates within the nanoparticle core become more negatively charged, thereby enhancing affinity for the dissolved ions. Furthermore, the elevation in pH could potentially lead to metal oxide and aggregate formation on the surface or within the particle, increasing the metal content further. Conversely, in the acidic protocol, pH adjustment occurred subsequent to the washing and filtration steps, thus eliminating the presence of free metal ions available for binding as the affinity increased.

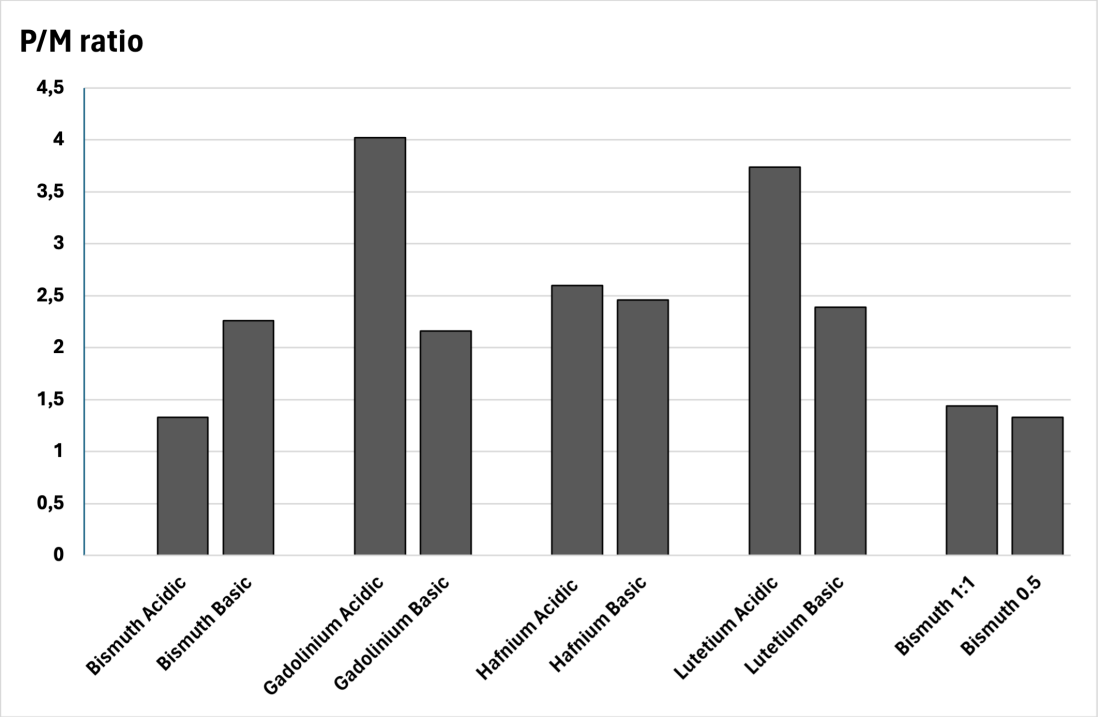

Fig. 5.1: Graph displaying the P/M ratio of the acidic and basic samples. Note that bismuth 1:1 and bismuth 0.5 were both prepared using the basic protocol.

Bismuth deviates from this trend with a ratio of 1.34 in the acidic protocol. After conducting multiple iterations of both ICP and DLS analyses, the conclusion was that this deviation likely stems from errors or anomalies during the loading process specific only to this sample. The target ratio of this sample was 2, and theoretically the ratio can not be lower than this. A lower ratio means that either there is a higher amount of metal in the sample than intended, or there was a lower amount of particles when the salts where added to the sample. This discrepancy suggests that the deviation may stem from inaccuracies in the process of weighing the salts. Another potential explanation is the accidental transfer of bismuth aggregates to the vials after centrifugation. We know that nanoparticles are lost during the metal-loading process, given the relatively low yield of all samples. This loss is likely occurring during filtration, where particles may adhere to surfaces or become trapped in pores. In samples where all metal ions are either dissolved or in a chelating site, the ratio would remain unaffected, since the unbound metal ions would be removed through filtration, and any lost nanoparticles would result in a proportional reduction in the metal content. However, aggregates are presumably large enough to be less inclined to this adhesion, resulting in bismuth clusters persisting throughout the process and leading to an abundance of bismuth oxides or bismuth metal compared to phosphorus in the final product.

These inconsistencies would probably go unnoticed without ratio analysis, and underscores the importance of ICP-OES in determining the accuracy and efficacy of our experimental procedures.

5.1.2 Size and Distribution Analysis

In this section, we delve into two distinct yet complementary techniques, Dynamic Light Scattering and Size Exclusion Chromatography to comprehensively characterize the dimensions and dispersity of the synthesized nanoparticles. Through the combination of these analytical approaches, we aim to gain a thorough understanding of the size, distribution, and aggregation behaviour of the nanoparticles, thereby assessing the success of the loading phase.

Dynamic Lights Scattering

The data acquired through DLS analysis generated graphical representations of the size distribution. Figure 5.2 illustrates a graph derived from the Tox Batch reference measurements. The results obtained from the DLS analysis are summarized in Table 5.1.

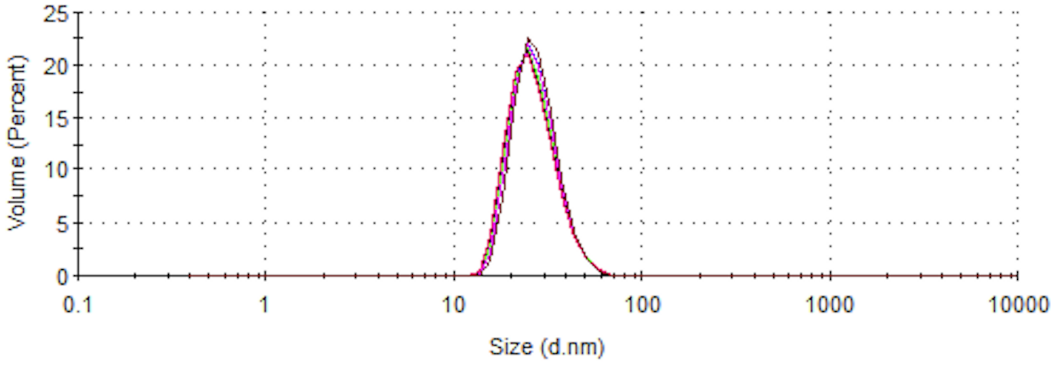

Fig. 5.2: Graph generated by DLS measurements of Tox Batch Reference sample. The graph illustrates seven separate overlapping measurements.

Table 5.1: Table over DLS data for acidic and basic samples, presenting mean hydrodynamic diameter for particles loaded with gadolinium, lutetium, hafnium, and bismuth, as well as a reference sample with unloaded Tox Batch. Note the deviating size of the acidic bismuth sample.

Dynamic Light Scattering		
Element	Acidic, Volume Mean (nm)	Basic, Volume Mean (nm)
Gadolinium	27.2	27.3
Lutetium	26.9	27.1
Hafnium	27.2	27.0
Bismuth	32.7	27.5
Reference	27.3	-

Ideally, the size of loaded particles should remain consistent with the original Tox Batch size. Assuming proper loading, all metal ions should be contained within the core's chelating sites, thereby maintaining the overall size. This has been observed in previous experiments on the particles. However, the bismuth prepared using the acidic protocol deviates by 20 % from the reference, which is a significant diameter variation.

Importantly, the DLS software offers different representations of data, with the information presented in Table 5.1 reflecting the volume mean. This metric represents an average size determined by the intensity and position of peaks in the data. Closer examination of the DLS measurement for the acidic bismuth sample reveals two distinct peaks. While the primary peak, aligns closely with anticipated values at approximately 27 nm, the additional peak emerges at around 4000 nm. As the software computes an average, this leads to a volume mean of 32.71 nm.

Typically, a value of this second peaks size would be dismissed as dust present in the cuvette, given the sample was filtered through a 0.2 µm filter. However, the absence of similar observations in other samples, coupled with the persistence of the peak across multiple iterations of the same sample, implies that dust is unlikely to be the causative factor. A more plausible explanation is that there are impurities like metal oxides or other aggregates present in the sample. This would also explain and be supported by the low metal-to-phosphorus ratio observed in ICP analysis. Considering the findings of DLS and ICP, it is very likely that the acidic bismuth samples contained some kind of bismuth clusters.

The persistence of these 4 µm impurities following filtration through the 0.2 µm filter may be due to the constraints of DLS rather than the filtration process. DLS, while reliable for assessing the average particle size, is susceptible to inaccuracies arising from particle aggregates and parameter settings. Additionally, the reliability decreases when particles vary significantly in size, owing to the exponential correlation between size and scattering. Hence, it is possible that the impurities are considerably smaller than 4 µm, but are misinterpreted by the DLS.

Notably, with the exception of bismuth, both protocols yield results with minimal impurities, contradicting the theoretical speculations regarding surface associated aggregates in 2.1.3. The basic protocol was anticipated to potentially contain more impurities due to the excess metal before pH adjustment, which could lead to aggregation and metal oxide formation on the surface. However, DLS measurements do not support this hypothesis, indicating that the metal ions are integrated into the particle core rather than forming aggregates on the coating. Consequently, both protocols are deemed suitable for metal loading.

Size Exclusion Chromatography

Figure 5.3 illustrates the chromatographic profile of the acidic bismuth and basic bismuth prepared using both protocols, superimposed on the measurements of the standards. This overlap allows for a direct comparison between the nanoparticle peaks and those of the standards. As anticipated, the peaks corresponding to the nanoparticles closely align with that of CPMV, which has a size of 28 nm. This finding was also true for the Lu, Gd and Bi samples. This supports the findings of the DLS analysis, confirming that the nanoparticles have an approximate size of 27 nm.

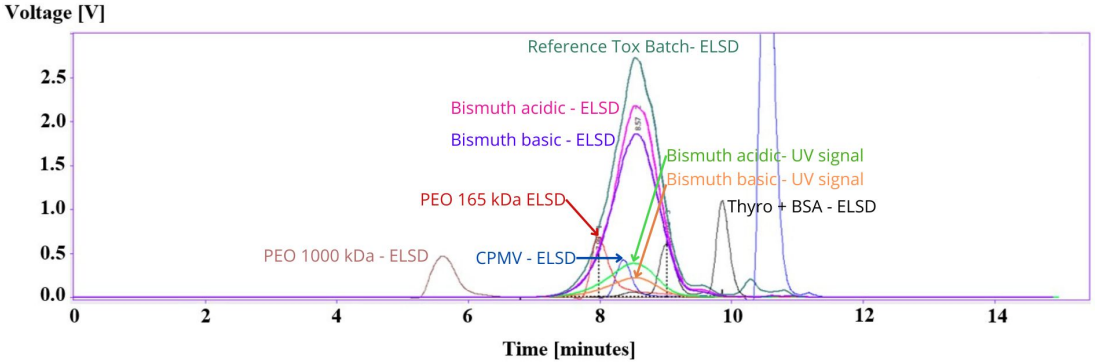

Fig. 5.3: Results from SEC analysis. Green - Tox Batch, Black - Thyro+BSA, Blue - CPMV, Red - PEO 165 kDa, Brown - PEO 1000 kDa, Dark red - Hf P1 and Magenta - Hf P2.

Moreover, in contrast to Dynamic Light Scattering, Size Exclusion Chromatography provides a heightened precision in discerning impurities. In Figure 5.4, we observe the presence of impurities highlighted in blue, particularly notable in the Tox batch. These impurities manifest with retention times ranging from 10 to 11 minutes, indicating sizes smaller than 7 nm, given their elution post-Bovine Serum Albumin (BSA). The impurities observed in the Tox batch have been previously identified. The left peak is attributed to coating constituents, likely resulting from spontaneous hydrolysis of the PEG coating. Conversely, the secondary peak arises from excipients, specifically glycerol, thioglycerol, and gentisic acid, deliberately included to enhance long-term stability by acting as antioxidants.

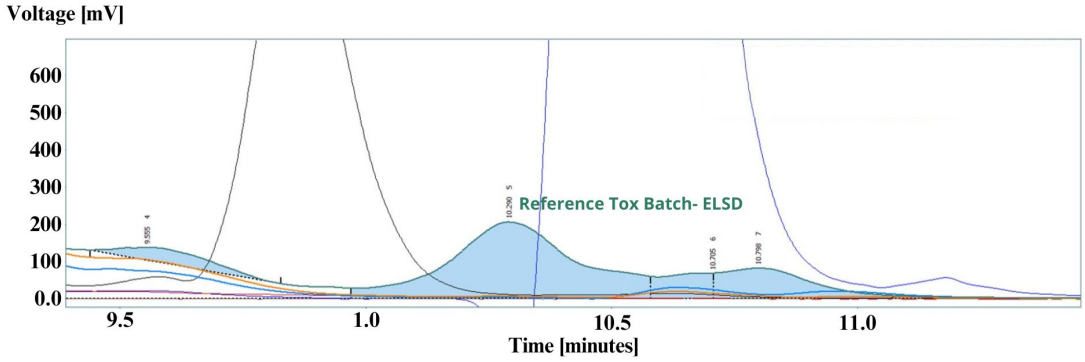

Fig. 5.4: Results from SEC analysis, focused on impurities. Blue highlight corresponds to contaminants in the Tox batch.

A comparison between the Tox batch reference and the metal-loaded nanoparticles reveals a significant decrease in impurities. This reduction is attributed to the washing and filtration processes employed, effectively removing accumulated contaminants resulting from coating hydrolysis, as well as the excipients.

The presence of impurities detected in the acidic bismuth sample via DLS was not confirmed by the SEC data. This observation is somewhat unexpected, but may be attributed to the aggregates being of a size that enables passage through the 0.2 µm filter, yet exceeds the capacity of the SEC column. The column utilized, Agilent bio SEC-5 1000Å 5 µm, is designed for the separation of biomolecules within a molecular weight range of 50,000 Da to 7,500,000 Da, roughly corresponding to 5 to 50 nm [28]. Hence, it is plausible that the aggregates fall within a size range smaller than 0.2 µm, allowing their passage through the syringe filter, but larger than 50 nm, rendering them incapable of passage through the HPLC column.

Beyond identifying impurities, SEC offers valuable insights into the size distribution of the nanoparticles. As expected, a distribution of sizes is observed, with an average size around 27 nm. The graph depicted in Figure 5.3 illustrates a very narrow distribution, indicating a high degree of uniformity among the nanoparticles and suggesting a relatively monodisperse population.

5.1.3 Morphology Examination

The TEM imaging sessions revealed a series of significant findings. The particle concentration utilized was based on previous TEM session conducted by Spago. However, as illustrated in Figures 5.5 and 5.6, it became apparent that this concentration yielded an excessively high particle count, resulting in unsatisfactory images. Even though it is possible to differentiate particles from each other, the vast majority appeared aggregated together, which makes morphology assessment unreliable.

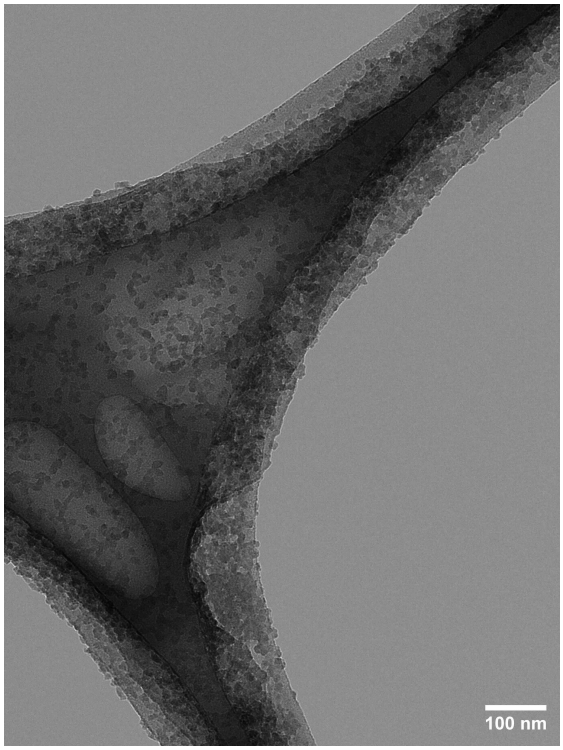

Fig. 5.5: Image of grid with high concentration of nanoparticles. The main structure is the lacey carbon grid supporting the particles. Different thickness leads to varying contrast across the grid. The small grains are the nanoparticles loaded with bismuth (Bi 0.5). The instrument is a JEOL Cryo-TEM 2200FS with an acceleration voltage of 120 kV.

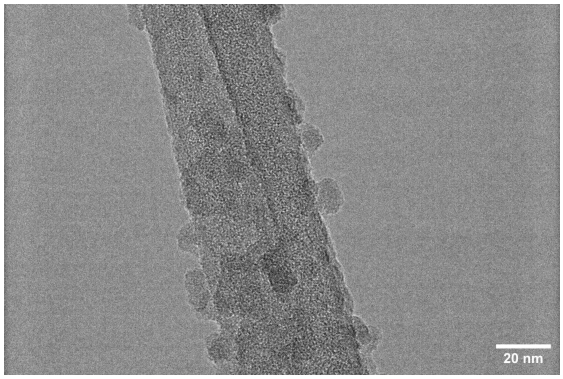

Fig. 5.6: TEM image taken with the 300 kV JEOL Analytical HR-TEM 3000F. Image depicts lutetium nanoparticles (Lu P2) at a concentration of 177 µM on a thin section of the lacey carbon film. Particles on the edge are clearly distinguishable, relatively spherical, and roughly the expected size.

The particles overlap and were difficult to distinguish, which greatly reduced the accuracy and ability to analyse the morphology of the particles. Consequently, in the following analysis, we diluted the sample by a factor 20 in an attempt to get optimal particle dispersion. As depicted in Figure 5.7, with the reduced concentration, we successfully captured images featuring solitary particles on the grid.

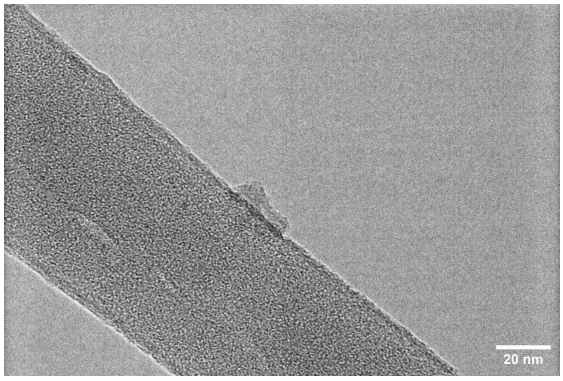

Fig. 5.7: TEM image taken with the 300 kV JEOL Analytical HR-TEM 3000F. Image depicts lutetium nanoparticles (Lu P2) at a concentration of 8.85 µM on a thin section of the lacey carbon film. The particle is deformed, most likely due to the increasing van der Waals forces as the solvent evaporates.

It is crucial to consider several factors during morphology examination and estimation of the particle size. Firstly, it is important to note that only the core of the particle is visible, since this is where the metal is situated and therefore dense enough to appear in TEM. This means that information about the outer polymeric layer is not gathered. Additionally, at the nanoscale, the influence of van der Waals forces significantly amplifies. This escalation arises from the exponential relationship between the magnitude of van der Waals forces and the distance separating two materials. At nanoscale dimensions, particularly in vacuum environments, particles tend to approach closer without being shielded by oxides, water, or other solvents. Consequently, van der Waals forces can exert a substantial influence, potentially causing significant deformation of the particles. As a result, it is likely that the particles are more spherical and smooth in solution than in the vacuum of the TEM. The deformation or flattening of particles, coupled with the limited provision of depth information may also lead to a potential overestimation of its size. Due to this fact, the particle size determined in the TEM should not be regarded as a precise measurement, but rather employed as a tool for particle identification. For exact size measurements we look at the DLS and SEC data.

Despite these caveats, the measurements gathered from the image remain valuable. Notably, the observation that the particle appears somewhat spherical and, most importantly, intact.

Unlike the lutetium particle in Figure 5.7, Figure 5.8 depicts an almost perfectly circular nanoparticle loaded with bismuth. The particle is most likely deformed in the direction perpendicular to, but not along, the surface. This leads to a much more uniform and smooth particle. The higher contrast is attributed to the lower acceleration voltage in the JEOL Cryo-TEM 2200FS discussed in 2.3.

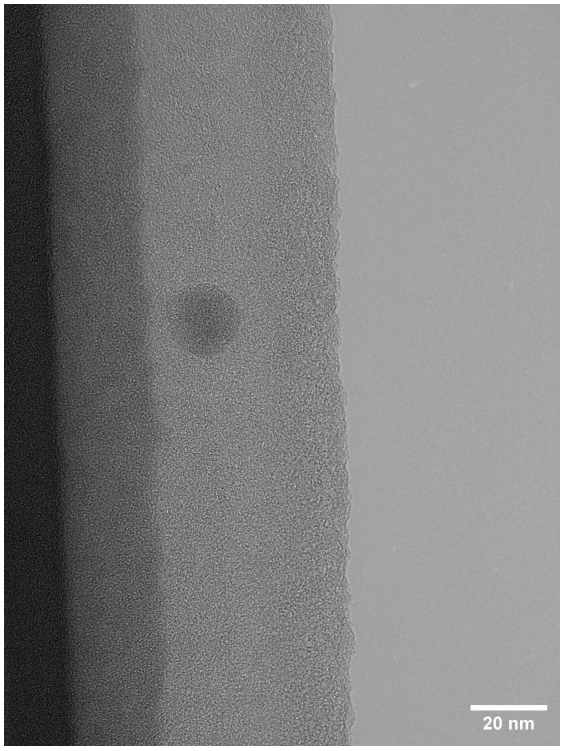

Fig. 5.8: Image of a nanoparticle close to the edge of the lacey carbon film. Different thickness leads to varying contrast across the lacey carbon film. The round feature depicts a spherical nanoparticle loaded with bismuth (Bi 0.5). The instrument is a JEOL Cryo-TEM 2200FS with an acceleration voltage of 120 kV.

The dark field STEM images provide a depiction of the particles with opposite contrast. The thicker and the higher the atomic number, the brighter it appears. Figure 5.9 showcases an individual particle in the bottom right corner that exhibits a high degree of spherical symmetry, making it one of the standout images captured during the analysis. These particles have high contrast due to the high degree of loading with bismuth. The other particles seem more deformed and some look aggregated.

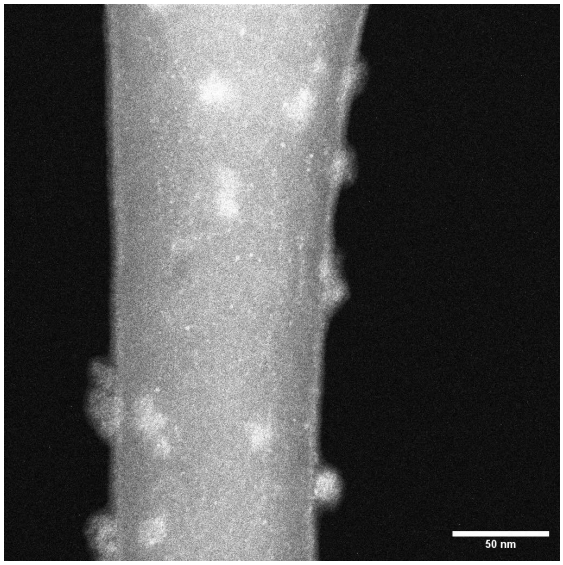

Fig. 5.9: High-Angle Annular Dark Field STEM image taken with the 300 kV JEOL Analytical HR-TEM 3000F. Image depicts nanoparticles loaded with bismuth (Bi 0.5) at a concentration of 8.85 µM on a thin section of the lacey carbon film. The particle in the bottom-right looks spherical and uniform.

During the imaging process of the heavily loaded Bi 0.5 sample, an observation was made: the particles appeared speckled, as depicted in Figure 5.10. The contrast is non-uniform, with apparent spots indicating areas of higher density within the particle structure.

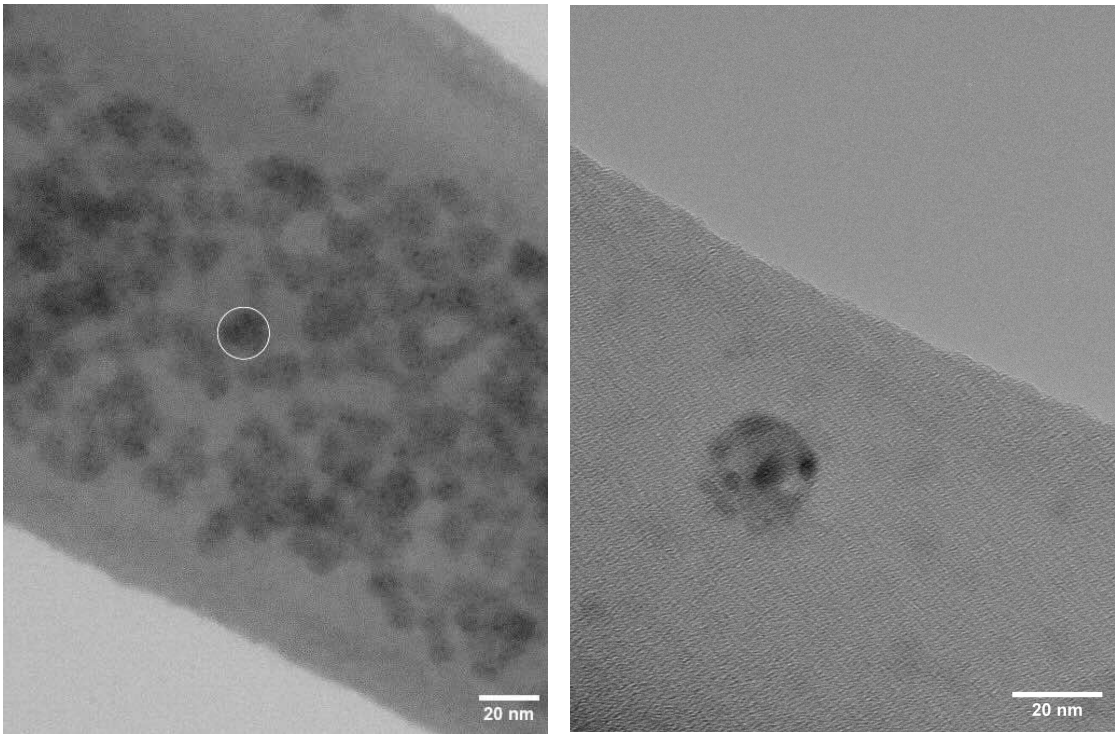

Fig. 5.10: Images of the highly loaded bismuth nanoparticles, taken using the instrument JEOL Cryo-TEM 2200FS with an acceleration voltage of 120 kV. (Left) Images of a region with a high particle concentration. The particles seem spotted or speckled. The white circle shows an individual particle. (Right) Close-up image of an individual particle from the same sample. The spotted appearance is clearly visible, indicating variation in density or thickness.

As this phenomenon was only observed for this higher loaded sample, the spotted appearance may be attributed to the exceptionally high metal concentration. One potential explanation for this is the presence of metal-ion rich pockets within the particle core. This may be the result of the increase in pH before washing and filtering the sample, which could cause surface-associated and dissolved metal to get drawn into the particle due to the relatively increased negative charge of the phosphonates. The change in pH could potentially also lead to aggregation and/or precipitation on the surface of the nanoparticles, which could appear as denser regions on the particle.

It is important to note that this specific sample has a phosphorus-to-metal ratio of 1.33, which is very low. As discussed in 2.1.3, each metal ion requires six phosphonates to have optimal binding. Consequently, a saturation point should be reached at a phosphorus-to-metal ratio of around 3. Although the random orientation of the monomers in the core may lead to a lower ratio, it is improbable that the ratio would reach much lower than 2. The observations made in Figure 5.10, therefore likely coincides with these spots resulting from precipitation or aggregation of metal or metal oxides. Notably, these particles were analyzed using DLS, and the average size coincides with the non-loaded Tox batch sample, suggesting that the aggregates are likely located inside the particle rather than on the surface.

During the TEM analysis, X-ray Energy-Dispersive Spectrometry was conducted on a region of the sample abundant with particles. This was done for the basic lutetium sample and yielded the results in Figure 5.11.

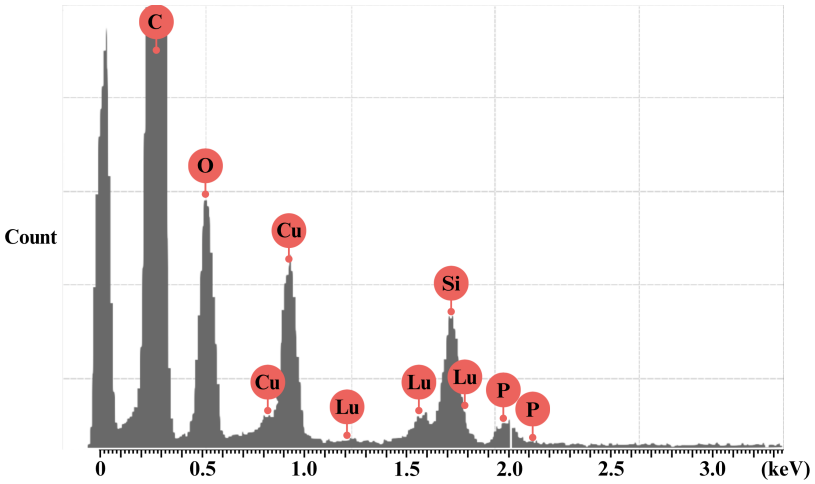

Fig. 5.11: Spectrometry graph generated by X-ray Energy-Dispersive Spectrometry. Each peak of detected X-rays corresponds to the orbital energy of an electron in a specific orbital of a specific element. The height of the peaks is the X-ray count. Peaks for Lu, Si, O, and P are likely generated from the sample particles. C peaks are predominantly from the carbon film and Cu peaks from the copper grid.

In X-ray energy dispersive spectrometry analysis (XEDS), each peak of detected X-rays corresponds to the orbital energy of a specific element within the sample, with the peak height reflecting their respective abundance. Notably, peaks attributed to Lu, Si, O, and P likely emanate from the particles themselves, in agreement with the expected elemental composition based on the ICP results. Background signals from C and Cu are inherent to TEM sample preparation and

predominantly originate from the carbon film and the copper grid.

ICP is highly accurate in determining elemental concentrations, whereas XEDS does not offer similar precision. As a result, this measurement rather serves as confirmation that the particle cores are indeed loaded with lutetium. In XEDS, the analysis is done on a targeted area, enabling precise measurement exclusively on the particles, whereas ICP encompasses the entirety of the sample. Thus, the XEDS results confirm the presence of lutetium within the particles, assuring that the lutetium is not present in some other aggregated form.

Figure 5.12 not only reveals a particle that has undergone deformation due to van der Waals forces, but also illustrates a phenomenon that can arise with high beam intensity in TEM. During acquisition, the beam was concentrated on the particle for an extended duration with high intensity, which appears to have resulted in the formation of a crystalline compound. This is caused by the energy transfer from the electron beam to the material and subsequent reactions. Observation of the bottom-left corner of the particle reveals discernible stripes or lines, indicating formation of atomic planes. Given the composition of the sample and relative abundance of C, P, Lu, O and Si, potential candidates for this compound include Lu_2O_3, graphite, SiC, pure Lu, LuP, or $LuSi_2$. Analysis of the interplanar distance yields a measurement of 3.2 Å between the atomic planes. Considering potential measurement errors and uncertainties, this value could theoretically correspond to any of the interplanar distances of the aforementioned compounds.

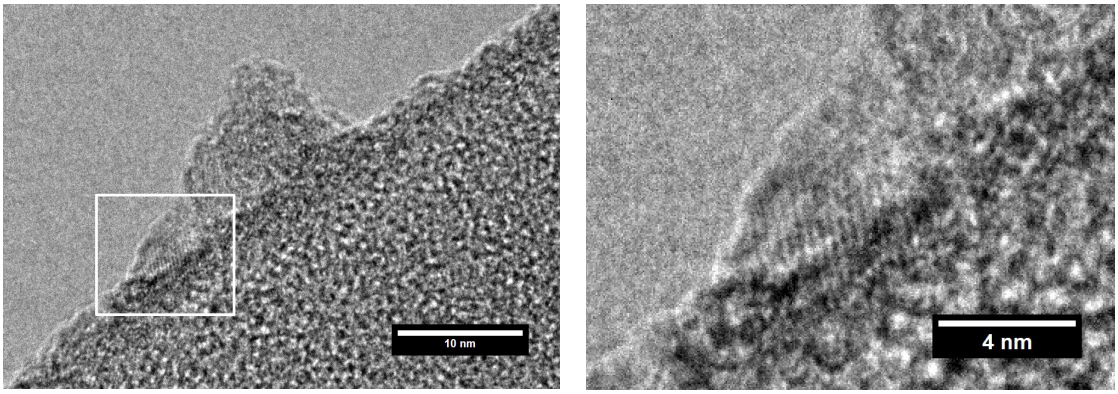

Fig. 5.12: (Left) 300 kV JEOL Analytical HR-TEM 3000F images of a Lu particle prepared using the basic protocol. The particle is clearly deformed, likely due to van der Waals forces. Bottom left of the particle exhibits stripes, indicating formation of a crystal structure. (Right) Image of the area contained in the white box, showing the atomic planes at higher magnification.

Firstly, it is well-documented that Lu exhibits a tendency to form Lu_2O_3 when subjected to heating in the presence of oxygen [29], rendering it one of the most probable candidates in this context. Alternatively, the image may depict pure crystallized lutetium metal, a hypothesis supported by the highly reducing nature of the electron beam. Graphite, while known to form during the heating of nanoparticles containing carbon, typically manifests as consecutive shells in the coating, suggesting that graphite is less probable in this instance.

Another viable candidate is SiC. The observed conditions are similar to a previous empirical finding at Spago. Challenges in nanoparticle combustion have arisen due to SiC formation on the surface, serving as a highly temperature-resistant coating. This theory is further supported by the extension of atomic planes from the core into the carbon film underlying the particle, suggesting that carbon plays a significant role in crystal formation. However, this observation could also be explained by the two-dimensional limitation discussed in 2.3. In other words, it is equally likely that the particle is partially positioned on top of the carbon film, creating the appearance of extension into the grid. Another point reducing the likelihood that the image depicts SiC is its interplanar distance of approximately 2.5 Å, which significantly deviates from the measured distance.

Finally, LuP and $LuSi_2$ represent rare lanthanide compounds with limited available information. Some studies discuss their stability, indicating that there is a possibility of their formation [30, 31]. However, most of these compounds form under high pressure, which is the opposite of the TEM conditions. This, in combination with the lack of comprehensive data, suggests that these compounds are unusual and unlikely to form. Collectively, the evidence discussed indicates that the crystalline compound is probably pure Lu or Lu_2O_3.

5.2 Cytotoxicity Assessment

The obtained fluorescence intensities were analyzed to assess the relative viability of the cell populations after exposure to the different samples. The results are illustrated in Figure 5.13.

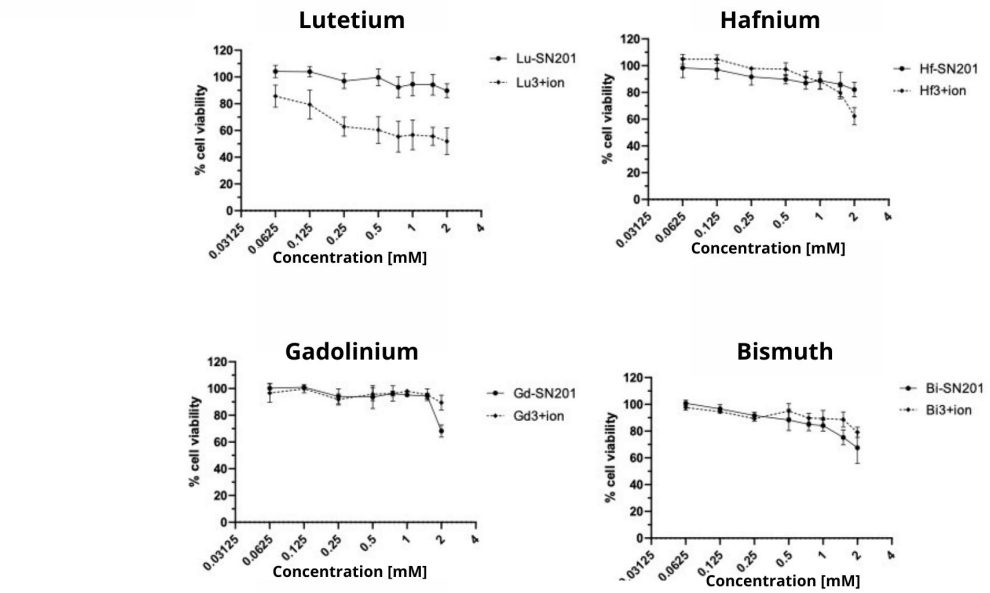

Fig. 5.13: Results obtained from three consecutive cytotoxicity assessments for each of the eight samples.

Comparative analysis between the metal-loaded nanoparticles and equivalent metal salt solutions only revealed a significant difference in cytotoxic profile for lutetium. These results show that lutetium ions are relatively cytotoxic at the employed concentrations, and that chelation to the nanoparticle significantly reduces the toxicity. Hafnium ions demonstrated marginal cytotoxic effects at elevated concentrations, whereas bismuth ions exhibited lower toxicity compared to

the respective loaded nanoparticles. The gadolinium nanoparticles and free ions exhibited comparable cytotoxicity across the entire range of concentrations, with the exception of the highest concentration where the nanoparticles showed higher toxicity than the ions. The variability in the results makes it difficult to draw definitive conclusions. With the exception of lutetium, the overall minimal difference in viability suggests similar cytotoxicity between all the samples and their respective free ions, indicating non-toxicity at the investigated concentrations.

Studies indicate different cytotoxic thresholds for the free metal ions used in this assessment, and there is no consensus on what concentration is toxic. Toxicity levels depend on multiple factors including cell line, concentration, potential oxide formation, and environmental variables. Ideally, increasing concentrations should provide insight into the dose-dependent cytotoxic nature, with increasing metal concentration correlating with progressive reduction in cell viability. Conventionally, cytotoxicity assessments involve incrementally raising concentrations until cell viability ceases, however, the attainable maximum concentration is constrained by the solubility equilibrium, beyond which aggregation and solid salt formation occurs. In other words, the dissolved concentration can not exceed a certain value, thereby preventing optimal execution of the assessment. This maximum was indeed reached for the bismuth salt solution, resulting in a cloudy and highly light scattering test solution. While sub-optimal, this approach was deemed the most effective for evaluating concentration-dependent toxicity. This phenomenon potentially explains the lack of concentration-dependent toxicity observed in the bismuth ion solution. Aggregated bismuth likely serves as a reservoir for bismuth ions, with new ions continuously being released as cells absorb the free ones, thereby maintaining a constant concentration of free ions in the solution. Although the risk of reaching maximum attainable concentration is relatively high for the free metal ions, nanoparticles have much higher solubility. As a consequence, future experiments should prioritize increasing nanoparticle concentrations rather than metal ion concentrations, to determine the threshold at which the particles manifest toxicity. Notably, the concentrations employed in this study far exceed what would be reached *in vivo*.

The negligible toxicity is also unsurprising, given that low toxicity was a fundamental criterion in selecting the elements. Moreover, the comparable non-toxicity between the metal ion solution and the particles suggests safety even if the ions were to dissociate from the particles. Based on these findings, the metal-loaded nanoparticles demonstrate minimal toxicity to cells and hold promise for *in vivo* studies.

It is likely that the loaded nanoparticles will indeed generate better image contrast compared to the old ones, due to the increased metal loading and the choice of element, both of which contribute to enhanced contrast. This increased contrast would enable a more precise visualization of particle distribution, facilitating a deeper understanding of their characteristics.

6 Conclusions

Through our characterization techniques, including ICP-OES, DLS, SEC, TEM imaging, and cytotoxicity assessment, we have gained valuable insights and data allowing evaluation of the success of incorporating higher atomic number metals into nanoparticles, as well as their safety for potential *in vivo* applications. Initially, our primary objective was to address the following question:

> *1. Can the loading of metal ions with high atomic number into the nanoparticles be successful to a degree that can be expected to yield greater contrast, and can they be effectively utilized in distribution studies, potentially outperforming existing methods?*

Yes, our results demonstrate successful loading of metal-ions into the nanoparticles, with varying degrees of success depending on the protocol used. The increased loading observed in nanoparticles prepared via the basic protocol supports the hypothesis that a higher pH prior to metal ion elimination increases the charge of phosphonates. This increased charge subsequently results in a stronger attractive force, facilitating the incorporation of ions into the nanoparticle core. With the exception of the acidic bismuth sample, the nanoparticles exhibited consistent size distribution and morphology, indicating that the incorporation of metal-ions did not significantly impact their functionally important properties. The consistent size also suggests that the increased loading in the basic protocol can be attributed to metal-ions within the particle core rather than surface associated metal oxides or aggregates. Given the substantial loading of metals and the high atomic number of the chosen elements, our findings suggest a successful enhancement of contrast in CT-scan and a satisfactory structural integrity and suitability for further studies.

With this prerequisite established, we seek to address the following question:

> *2. What is the toxicity profile of the synthesized metal-loaded nanoparticles, and can the safety and efficacy of these loaded particles for in vivo applications be confirmed?*

Yes, cytotoxicity assessments revealed minimal toxicity of the metal-loaded nanoparticles, with comparable or better profiles to equivalent metal salt solutions. These findings underscore the safety of the nanoparticles for potential *in vivo* applications, providing a solid foundation for future studies. However, further comprehensive evaluations, including biocompatibility and long-term effects, are necessary to confirm their safety *in vivo*.

Moving forward, the enhanced contrast properties of the metal-loaded nanoparticles hold promise for more accurate visualization of particle distribution *in vivo*, facilitating a deeper understanding of their characteristics and potential therapeutic efficacy. Additionally, comprehensive evaluations of biocompatibility, pharmacokinetics, immunogenicity, and long-term effects will be crucial in guiding further development.

A. Appendix

Table A.1.: Table of settings used during ICP.

Parameter	**Setting**
No. of repliactes	2
Sample uptake delay time (s)	55
Instrument Stabilization time (s)	20
Replicate read time (s)	5
Plasma gas flow (L/min)	15 °C
Auxillary gas flow (L/min)	1.5
RF power (kW)	1.2
Nebulizer flow (L/min)	0.75
Flow rate of peristaltic pump (rpm)	15
Wash between samples	Rinse 35s with 1% HNO3

Table A.2.: Table over standards A-E used for ICP elemental analysis and resulting concentrations for Gadolinium, Lutetium, Hafnium and Bismuth.

Standards for ICP — Resulting Concentration						
Dilution	Si (mg/L)	P (mg/L)	Bi (mg/L)	Gd (mg/L)	Hf (mg/L)	Lu (mg/L)
A	10.1034	10.04	8.03114	8.02475	7.9285	0.63563
B	3.36781	3.34667	2.67705	2.67492	2.64283	0.21188
C	1.12260	1.11556	0.89235	0.89164	0.88094	0.07063
D	0.374200	0.37185	0.29745	0.29721	0.29365	0.02354
E	0.187100	0.18593	0.14872	0.14861	0.146820	0.01177

Table A.3.: Table of settings used during dynamic light scattering analysis.

Parameter	**Setting**
Refractive index of sample	1.59
Absorption of sample	0.010
Dispersant	Water
Viscosity of dispersant	0.8872 cP
Temperature	25 °C
Refractive index of dispersant	1.33
Equilibration time	120 seconds
Number of measurements	7
Number of runs	11
Duration per run	10 seconds

Table A.4.: Settings and material used for SEC analysis.

Parameter	**Settings/Material**
Coloumn	Agilent bio SEC-5 1000Å 5 µm
Coloumn temp	Ambient
Mobile Phase	50 mM [NH4CH;CO2] + 10% v/v acetonitrile + water
Flow	1.2 mL/min
Injection Volume	10 µL
ELSD Detector	60 °C; 1.2 L/min; Gain=4
UV Detector	230 nm; 280 nm; 350 nm

Table A.5.: Table displaying all results from DLS analysis. Each value given in the report is an average of these measurements.

Dynamic Light Scattering			
Element/Protocol 1	Volume Mean (nm)	Element/Protocol 2	Volume Mean (nm)
Gd 1	27.29	Gd 1	27.21
Gd 2	26.8	Gd 2	27.4
Gd 3	27.2	Gd 3	27.17
Gd 4	26.78	Gd 4	27.36
Gd 5	27.41	Gd 5	27.26
Gd 6	27.76	Gd 6	27.04
Gd 7	27.57	Gd 7	27.43
Lu 1	26.78	Lu 1	27.46
Lu 2	26.81	Lu 2	26.89
Lu 3	26.87	Lu 3	27.12
Lu 4	27.11	Lu 4	26.95
Lu 5	27.07	Lu 5	27.03
Lu 6	26.88	Lu 6	26.85
Lu 7	26.81	Lu 7	27.49
Hf 1	27.02	Hf 1	26.8
Hf 2	27.42	Hf 2	27.18
Hf 3	27.39	Hf 3	27.55
Hf 4	27.43	Hf 4	26.5
Hf 5	26.7	Hf 5	26.9
Hf 6	27.29	Hf 6	27.01
Hf 7	26.87	Hf 7	27.4
Bi 1	26.43	Bi 1	27.71
Bi 2	29.25	Bi 2	26.95
Bi 3	34.75	Bi 3	27.95
Bi 4	27.41	Bi 4	26.92
Bi 5	36.78	Bi 5	28.07
Bi 6	38.91	Bi 6	27.65
Bi 7	35.45	Bi 7	27.39
Tox batch ref 1	27.17	-	-
Tox batch ref 2	27.26	-	-
Tox batch ref 3	27.47	-	-
Tox batch ref 4	26.94	-	-
Tox batch ref 5	26.7	-	-
Tox batch ref 6	27.54	-	-
Tox batch ref 7	27.95	-	-

Table A.6.: Preparation of SEC mobile phase.

Ammonium Acetate [NH4CH3CO2]	
Mass of NH4c (g)	3.85
Volume of H2O (L)	0.9
Concentration (mM)	50 mM + 10 % CAN
pH	6.7
Acetonitrile (HPLC grade) (L)	0.1
Sonicated (Y/N)	Y

Table A.7.: Table over dilutions and retention time for all standards used in SEC.

			Dilution 1 in 50 mM buffer	Dilution 2 in mobile phase	
	Batch	Lot	Concentration (mg/L)	Concentration (mg/mL)	Rt (min)
CPMV	161118		1.00	CPMV injected directly	8.36
Peo 1000k	0006432284	0006432284	5.14	1.03	5.6
PEO 165k	03222021	peo280708wa	6.10	1.22	7.98
Thyro	609310-100MG	34344670	4.40	1.32	9.02
BSA	05470-1G	SLCB7618	4.30	0.86	9.87

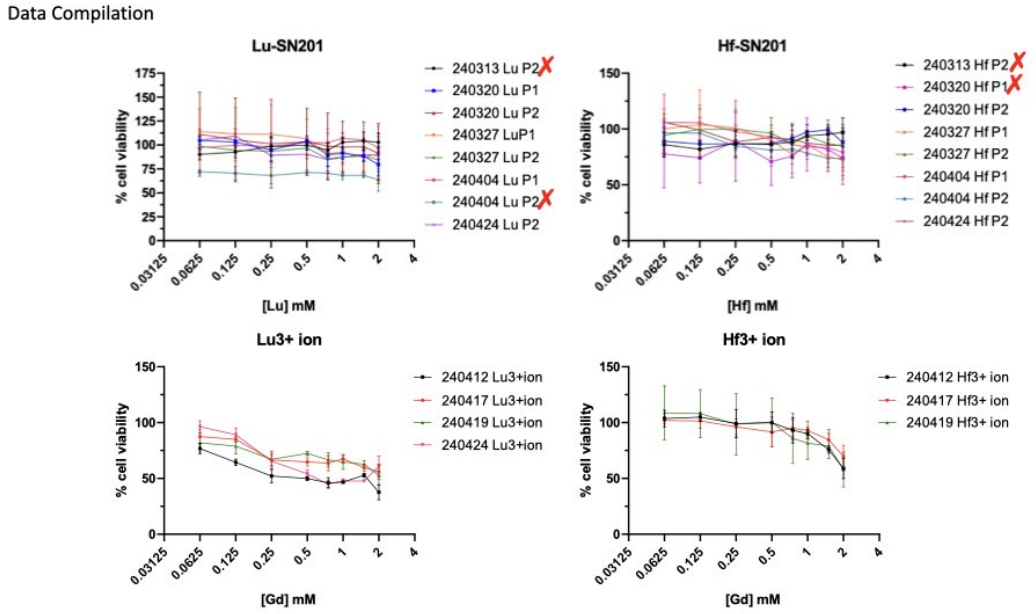

Fig. A.1.: Graphs displaying more detailed results from cytotoxicity assessment. Graphs in the report is an average of these values. SN201 is the name for the nanoparticles.

Table A.8.: Table over Acidic and Basic samples - ICP elemental analysis with concentrations for Phosphorus (P), metals (gadolinium, lutetium, hafnium and bismuth), and ratio between phosphorus and metal for each sample.

Inductive Coupled Plasma Optical Emission Spectrometry			
Element/Protocol	Concentration P (mM)	Concentration Metal (mM)	P/Metal Ratio
Gadolinium Acidic	35.04	8.72	4.02
Gadolinium Basic	48.0	22.3	2.16
Lutetium Acidic	32.6	8.7	3.74
Lutetium Basic	44.3	18.51	2.39
Hafnium Acidic	34.0	13.08	2.60
Hafnium Basic	38.4	15.62	2.46
Bismuth Acidic	39.02	28.22	1.33
Bismuth Basic	114.92	49.62	2.26
Bi 1	20.3	14.07	1.44
Bi 0.5	19.0	14.36	1.33

Table A.9.: Table of results for acidic and basic bismuth, displaying retention times, area fractions, concentration and volumes of interest. Bi P1 is the bismuth prepared using the acidic protocol and Bi P2 is prepared using the basic protocol.

					Main Fraction	Area fraction (%)			Rt (min)	Rt (min)
ELSD-signal	ID	Dilution in blank (mobile phase)	[P] (mM) after dilution	Injection V (µL)	Rt (min)	Larg Fraction	Main Fraction	Small Fraction	Shoulder peak	Impurities
Green trace:	Tox 60 mM P	3	20	10	8.54	7.1	85.3	7.7	9.56	10.3-10.71-10.8
Pink trace:	Bi-P1 39 mM P	2	19.5	10	8.53	5.9	86.5	7.6	NA	10.62-10.94
Purple trace:	Bi-P1 115 mM P	6	19.17	10	8.57	6.9	85.7	7.5	NA	10.63-10.93

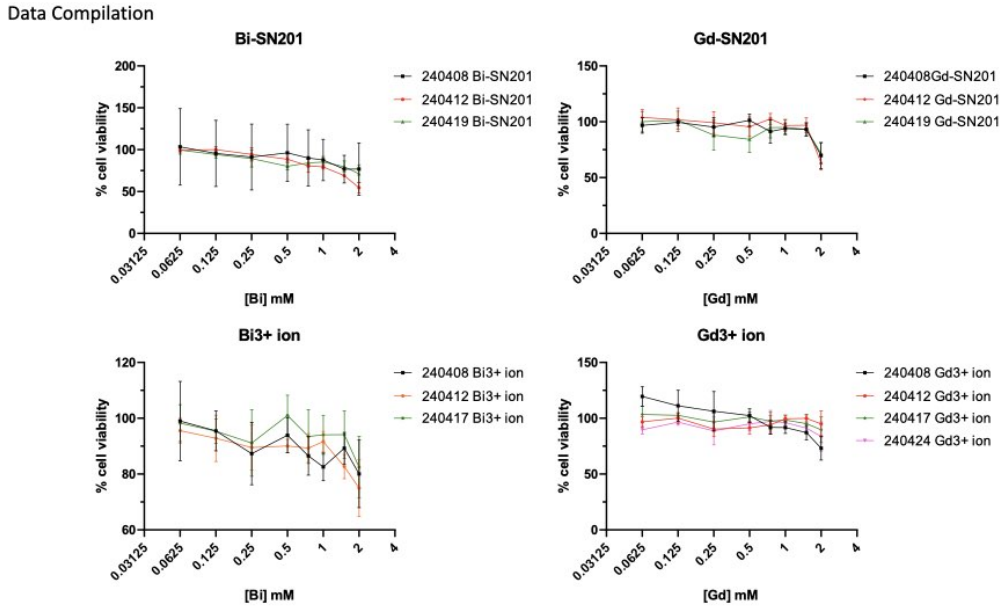

Fig. A.2.: Graphs displaying more detailed results from cytotoxicity assessment. Graphs in the report is an average of these values. SN201 is the name for the nanoparticles.

Table A.10.: Table of results for acidic and basic gadolinium, displaying retention times, area fractions, concentration and volumes of interest. Gd P1 is the gadolinium prepared using the acidic protocol and Gd P2 is prepared using the basic protocol.

					Main Fraction	Area fraction (%)			Rt (min)	Rt (min)
ELSD-signal	ID	Dilution in blank (mobile phase)	[P] (mM) after dilution	Injection V (µL)	Rt (min)	Larg Fraction	Main Fraction	Small Fraction	Shoulder peak	Impurities
Green trace:	Tox 60 mM P	3	20	10	8.54	7.1	85.3	7.7	9.56	10.3-10.71-10.8
Pink trace:	Gd-P1 35.1 mM P	2	17.55	10	8.53	6.4	85.9	8.2	9.54	10.64-10.94
Purple trace:	Gd-P2 48.1 mM P	2	24.05	10	8.60	6.6	85.2	8	9.54	10.61

Table A.11.: Table of results for acidic and basic hafnium, displaying retention times, area fractions, concentration and volumes of interest. Hf P1 is the hafnium prepared using the acidic protocol and Hf P2 is prepared using the basic protocol.

					Main Fraction	Area fraction (%)			Rt (min)	Rt (min)
ELSD-signal	ID	Dilution in blank (mobile phase)	[P] (mM) after dilution	Injection V (µL)	Rt (min)	Larg	Main	Small	Shoulder peak	Impurities
Green trace:	Tox 60 mM P	3	20	10	8.54	7.1	85.3	7.7	9.56	10.3-10.71-10.8
Pink trace:	Hf-P1 43 mM P	2	17	10	8.62	7	85.6	7.4	NA	10.64-10.92
Purple trace:	Hf-P2 38.4 mM P	2	19.2	10	8.60	7.5	84.4	8.1	NA	10.64-10.93

Table A.12.: Table of results for acidic and basic lutetium, displaying retention times, area fractions, concentration and volumes of interest. Lu P1 is the lutetium prepared using the acidic protocol and Lu P2 is prepared using the basic protocol.

					Main Fraction	Area fraction (%)			Rt (min)	Rt (min)
ELSD-signal	ID	Dilution in blank (mobile phase)	[P] (mM) after dilution	Injection V (µL)	Rt (min)	Larg Fraction	Main Fraction	Small Fraction	Shoulder peak	Impurities
Green trace:	Tox 60 mM P	3	20	10	8.54	7.1	85.3	7.7	9.56	10.3-10.71-10.8
Pink trace:	Lu-P1 32.6 mM P	2	16.3	10	6.61	6.7	85.9	7.4	NA	10.63-10.96
Purple trace:	Lu-P2 44.3 mM P	2	22.15	10	8.65	6.1	85.2	8.7	NA	10.64-10.98

References

[1] NIH National Cancer Intitute. *Cancer Statistics*. 25-09-2020. URL: https://www.cancer.gov/about-cancer/understanding/statistics (visited on 05/06/2024).

[2] Rebecca L. Seigel et al. "Cancer Statistics, 2023". In: *CA Cancer J Clin* 73 (1) (2023), pp. 17–48. DOI: 10.3322/caac.21763.

[3] H. Maeda. *The 35th Anniversary of the Discovery of EPR Effect: A New Wave of Nanomedicines for Tumor-Targeted Drug DeliveryPersonal Remarks and Future Prospects*. 11(3), 229. Journal of Personalized Medicine, 2021. DOI: 10.3390/jpm11030229.

[4] Spago Nanomedical AB. *Technology*. 2024. URL: https://spagonanomedical.se/technology/ (visited on 02/06/2024).

[5] Ingrid Yao Mattisson et al. *Characterization and Efficacy of a Nanomedical Radiopharmaceutical for Cancer Treatment*. 8 (2), 2357-2366. ACS Omega, 2023. DOI: 10.1021/acsomega.2c06755.

[6] Jung Soo Suk et al. *PEGylation as a strategy for improving nanoparticle-based drug and gene delivery*. 99, 28– 51. Advanced Drug Delivery Reviews, 2016. DOI: 10.1016/j.addr.2015.09.01213.

[7] Joachim Nölte. *ICP Emission Spectrometry, A Practical Guide*. Wiley-VCH, 2003. ISBN: 978-3-527-30672-5.

[8] Patrícia M. Carvalho et al. "Application of Light Scattering Techniques to Nanoparticle Characterization and Development". In: *Frontiers in Chemistry* 6 (June 2018). DOI: 10.3389/fchem.2018.00237.

[9] Stetefeld J, McKenna SA, and Patel TR. "Dynamic light scattering: A practicle guide and applications in biomedical sciences". In: *Biophys Rev* 8(4) (Dec. 2016), pp. 409–427. DOI: 10.1007/s12551-016-0218-6.

[10] Thermo Fisher Scientific. *HPLC Basics*. 2024. URL: https://www.thermofisher.com/se/en/home/industrial/chromatography.html (visited on 02/09/2024).

[11] Martin Hall. *Biopharmaceutical Processing*. Ed. by Günter Jagschies et al. Elsevier, 2018. Chap. 21 - Size Exclusion Chromatography (SEC), pp. 421–432. ISBN: 9780081006238. DOI: 10.1016/B978-0-08-100623-8.00021-9.

[12] Leopold K Kostanski, Douglas M Keller, and Archie E Hamielec. "Size-exclusion chromatography—a review of calibration methodologies". In: *Journal of Biochemical and Biophysical Methods* 58 (2) (Feb. 2004), pp. 159–186. DOI: 10.1016/j.jbbm.2003.10.001.

[13] K. Quigley R.G. Leonard. *Adhesives and Sealants*. Ed. by Colin Poole Paul Worsfold Alan Townshend. Elsevier, 2005, pp. 28–37. ISBN: 9780123693976. DOI: 10.3390/jpm11030229.

[14] Xun Yan. *Carbohydrate Analysis by Modern Liquid Phase Separation Techniques (Second Edition)*. Ed. by Ziad El Rassi. Elsevier, 2021. Chap. 14 - Carbohydrate analysis by high-performance liquid chromatography (HPLC) with evaporative light-scattering detection (ELSD), pp. 631–644. ISBN: 9780128214473. DOI: 10.1016/B978-0-12-821447-3.00013-5.

[15] Iqbal Jalaludin and Jeongkwon Kim. “Comparison of ultraviolet and refractive index detections in the HPLC analysis of sugars”. In: *Food Chemistry* 365 (Dec. 2021). DOI: 10.1016/j.foodchem.2021.130514.

[16] David B Williams and C Barry Carter. *Transmission Electron Microscopy: A Textbook for Materials Science*. Second Edition. Springer, 2009. ISBN: 978-0-387-76501-3. DOI: 10.1007/978-0-387-76501-3.

[17] R F Egerton. “Choice of operating voltage for a transmission electron microscope”. In: *Ultramicroscopy* 145 (Oct. 2014), pp. 85–93. DOI: 10.1016/j.ultramic.2013.10.019.

[18] Miguel Tinoco, María Pilar Yeste, and Marta Sendra. *Nano-enabled Agrochemicals in Agriculture*. Academic Press, 2022, pp. 79–104. ISBN: 978-0-323-91009-5. DOI: 10.1016/B978-0-323-91009-5.00007-0.

[19] Ernest Rutherford. “LXXIX. The scattering of and particles by matter and the structure of the atom”. In: *Philosophical Magazine* (July 1911), pp. 669–688. DOI: 10.1080/14786440508637080.

[20] Bartłomiej Taciak et al. “Evaluation of phenotypic and functional stability of RAW 264.7 cell line through serial passages”. In: *PLOS ONE* (June 2018). DOI: 10.1371/journal.pone.0198943.

[21] Robert B. Brown and Julie Audet. “Current techniques for single-cell lysis”. In: *Journal of The Royal Society Interface* (Apr. 2008). DOI: 10.1098/rsif.2008.0009.focus.

[22] M Aránzazu Partearroyo et al. “Surfactant-induced cell toxicity and cell lysis: A study using B16 melanoma cells”. In: *Biochemical Pharmacology* 40.6 (Sept. 1990), pp. 1323–1328. DOI: 10.1016/0006-2952(90)90399-6.

[23] Promega. *CellTiter-Blue® Cell Viability Assay*. 2023. URL: https://se.promega.com/-/media/files/resources/protocols/technical-bulletins/101/celltiter-blue-cell-viability-assay-protocol.pdf?rev=3313091698e544ceaa6fff843658eb84&sc_lang=en.

[24] Kevin Apmann et al. “Thermal Conductivity and Viscosity: Review and Optimization of Effects of Nanoparticles”. In: *Materials* (Mar. 2021). Ed. by Paola Ammendola. DOI: 10.3390/ma14051291.

[25] John Innes Centre. “Cowpea Mosaic Virus”. In: *Encyclopedia of Virology* (July 2008), pp. 569–574. DOI: 10.1016/B978-012374410-4.00562-8.

[26] Siew E.L. et al. “In vitro toxicological assessment of gadolinium (III) chloride in V79–4 fibroblasts”. In: *Genes and Environment* 42 (June 2020). DOI: 10.1186/s41021-020-00161-3.

[27] Friebe B. et al. “The potential toxic impact of different gadolinium-based contrast agents combined with 7-T MRI on isolated human lymphocytes”. In: *Eurpean Radiology Experimental* 2 (Oct. 2018). DOI: https://doi.org/10.1186/s41747-018-0069-y.

[28] Agilent. *Agilent Bio SEC-5 LC Columns Data Sheet*. 2021. URL: https://www.agilent.com/cs/library/datasheets/public/5973-1743.pdf.

[29] N.N. Greenwood and A. Earnshaw. *Chemistry of the Elements*. Second Edition. Elsevier Butterworth-Heinemann, 1997, pp. 1235–1236. ISBN: 978-0-7506-3365-9. DOI: 10.1016/C2009-0-30414-6.

[30] Dr. Sunil Singh Chouhan et al. “High Pressure Phase Transition and Elastic Properties of Lutetium Monopnictides”. In: *AIP Conference Proceedings* (July 2011). DOI: 10.1063/1.3605755.

[31] Gitanjali Pagare et al. “First principles study of structural, electronic and elastic properties of lutatium mono-pnictides”. In: *Computational Materials Science* 50.2 (Dec. 2010), pp. 538–544. DOI: 10.1016/j.commatsci.2010.09.016.